Interaction of Folic Acid with Nanocrystalline Apatites and Extension to Methotrexate (Antifolate) in View of Anticancer Applications

Stéphanie Sarda,[*,†] Michele Iafisco,[*,‡] Patricia Pascaud-Mathieu,[†,∥] Alessio Adamiano,[‡] Monica Montesi,[‡] Silvia Panseri,[‡] Olivier Marsan,[†] Carole Thouron,[†] Agnès Dupret-Bories,[†,§] Anna Tampieri,[‡] and Christophe Drouet[*,†,‡]

[†]CIRIMAT, Université de Toulouse, CNRS, 31030 Toulouse, France

[‡]Institute of Science and Technology for Ceramics (ISTEC), National Research Council (CNR), Via Granarolo 64, 48018 Faenza, Italy

[§]Chirurgie ORL et cervico-faciale, Institut Claudius Regaud, Institut Universitaire du Cancer de Toulouse Oncopole (IUCT-O), Toulouse 31052, France

ABSTRACT: Nanocrystalline apatites mimicking bone mineral represent a versatile platform for biomedical applications thanks to their similarity to bone apatite and the possibility to (multi)functionalize them so as to provide "à la carte" properties. One relevant domain is in particular oncology, where drug-loaded biomaterials and engineered nanosystems may be used for diagnosis, therapy, or both. In a previous contribution, we investigated the adsorption of doxorubicin onto two nanocrystalline apatite substrates, denoted HA and FeHA (superparamagnetic apatite doped with iron ions), and explored these drug-loaded systems against tumor cells. To widen their applicability in the oncology field, here we examine the interaction between the same two substrates and two other molecules: folic acid (FA), often used as cell targeting agent, and the anticancer drug methotrexate (MTX), an antifolate analogue. In a first stage, we investigated the adsorptive behavior of FA (or MTX) on both substrates, evidencing their specificities. At low concentration, typically under 100 mmol/L, adsorption onto HA was best described using the Sips isotherm model, while the formation of a calcium folate secondary salt was evidenced at high concentration by Raman spectroscopy. Adsorption onto FeHA was instead fitted to the Langmuir model. A larger adsorptive affinity was found for the FeHA substrate compared to HA; accordingly, a faster release was noticed from HA. In vitro tests carried out on human osteosarcoma cell line (SAOS-2) allowed us to evaluate the potential of these compounds in oncology. Finally, in vivo (subcutaneous) implantations in the mouse were run to ascertain the biocompatibility of the two substrates. These results should allow a better understanding of the interactions between FA/MTX and bioinspired nanocrystalline apatites in view of applications in the field of cancer.

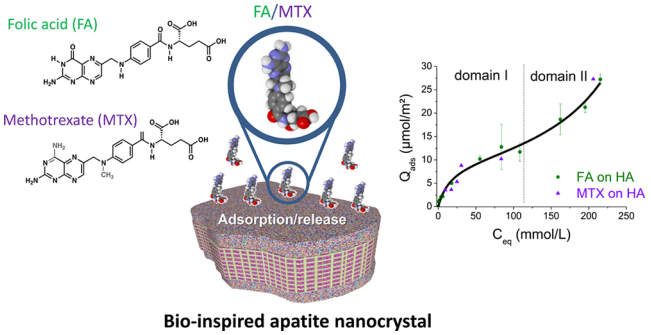

Bio-inspired apatite nanocrystal

1. INTRODUCTION

Calcium phosphates have attracted attention for decades in the biomaterials field, especially for bone repair applications.[1−4] In this view, apatitic compounds are of particular significance as they are naturally present in bones and teeth of which they constitute the mineral component.[5] However, in bone and dentin, apatite crystals differ significantly from the well-known stoichiometric hydroxyapatite (HA), $Ca_{10}(PO_4)_6(OH)_2$, often encountered as bone replacement bioceramics, in that they are nonstoichiometric (involving calcium and hydroxide vacancies), but also are nanosized, hydrated and exhibit specific surface features.[6,7] Interestingly, these characteristics can be mimicked and tailored synthetically, employing adequate soft chemistry routes such as low/moderate temperature precipitation methods,[8−13] hydrothermal synthesis,[14−16] sol−gel,[17−19] vapor diffusion,[20,21] emulsion-based processes,[22] among others. The as-obtained materials are usually called biomimetic or nanocrystalline apatites.

Nowadays, the synthesis of biomimetic apatites, their processing, and associations with drugs constitutes a large domain of investigation worldwide, aiming to exploit further the fascinating properties of these compounds, including their "intrinsic" biocompatibility, biodegradability, bioactivity, and high surface reactivity.[5,23] The latter in particular allows associating a great variety of biomolecules or drugs with apatite

DOI: 10.1021/acs.langmuir.8b02602

nanocrystals by adsorptive processes; and several examples have been reported in recent years involving antibiotics,[24−26] monoclonal antibodies,[27] bisphosphonates,[28,29] anticancer drugs,[30−33] hemostatic agents,[34] antibacterial enzymes,[35] and DNA and nucleotides.[36−41] Such nanocrystalline apatites can be either processed to form "bulk" biomaterials, or dense slurry generally for bone repair applications, but also in the form of suspensions of individual nanoparticles for applications in "nanomedicine" such as for the setup of drug nanocarriers or nanoprobes for medical imaging (e.g., via fluorescence marking). In the latter domains, recently, nanocrystalline apatite nanoparticles have, for example, been used to deliver in vitro doxorubicin (DOX) to osteosarcoma cells,[30] and for the cryopreservation of erythrocytes (red blood cells)[42] where their ability to interact with cell membranes was exploited.

Research with apatite nanoparticles as novel nanosystems is in particular appealing in the field of cancer therapy or diagnosis. In the present research work, we focused on two types of nanocrystalline apatite compounds, raw or associated with iron for conferring superparamagnetic properties useful for hyperthermia, magnetic particle guidance, and imaging by MRI.[30,43−45] The sorption behavior of folic acid (FA) on these two substrates was explored here from a physicochemical viewpoint for these two substrates. FA is indeed an interesting biomolecule in the field of oncology, as it may act as a cell-targeting agent for addressing nanocarriers more specifically toward cells overexpressing folate receptors (FR), as in some breast or ovary cancers.[46] Besides, other relevant uses of FA-functionalized apatite particles can be found as in bone regeneration where it is possible to exploit an enhanced osteoblastic differentiation effect.[47] Cell targeting capability of FA-functionalized nanosystems was reported (e.g., from Sun et al.[48]) and the increased cell addressing capacity of colloidal apatite nanoparticles was pointed out previously[49] using T-47-D breast cancer cells as model FR^+ cells.

The possibility to master and understand underlying sorption mechanisms for FA on these two bioinspired apatites is one objective of the present contribution, since it would clarify the mode of interaction between bioactive FA molecules and nanocrystalline apatitic compounds intended for medical use. Although interaction between FA and calcined, well-crystallized hydroxyapatite has been the object of a previous study,[50] the use of low-temperature, bone-like nanocrystalline apatites as substrates for FA sorption has not yet been explored in detail. In addition, this study may allow to extrapolate the adsorption behavior of antifolate agents, such as the chemotherapy drug methotrexate (MTX) which is also recognized by folate receptors,[51] thus opening novel therapeutic perspectives for anticancer drug nanocarriers. This proof of principle was explored in the present work, and in vitro tests were carried out, to examine efficacy on osteosarcoma cell death.

2. EXPERIMENTAL SECTION

This study follows a work dedicated to the exploration of the interaction of DOX with either iron-doped (denoted FeHA) and undoped (denoted HA) nanocrystalline apatite particles.[30] The same two apatite substrates were used here for investigating the interaction with folic acid (FA) or methotrexate (MTX), thus allowing also comparisons of sorptive behaviors between DOX and FA/MTX. The preparation of these two apatite substrates was thus described elsewhere.[30] However, for the sake of completeness, the synthesis protocols have also been recalled again below.

2.1. Synthesis of Undoped Biomimetic Nanocrystalline Apatite (HA). The undoped nanocrystalline apatite sample (noted HA in this study) was obtained via double decomposition at room temperature and physiological pH (~7.4) by contacting an aqueous solution of calcium nitrate (52.2 g $Ca(NO_3)\cdot 4H_2O$ in 750 mL) with a carbonate and phosphate aqueous solution (165.8 g of $(NH_4)_2HPO_4$ and 9.0 g of $NaHCO_3$ in 1500 mL). The precipitate was matured in the reaction medium for 24 h at 50 °C, and then filtered, washed with deionized water, and freeze-dried. The retrieved powder sample was sieved (<125 μm) and stored at −18 °C for avoiding any possible alteration prior to use.

2.2. Synthesis of Superparamagnetic Iron-Doped Nanocrystalline Apatite (FeHA). Iron-doped apatite (denoted FeHA in this study) was prepared following a previously set up methodology[52] where a H_3PO_4 aqueous solution (44.4 g in 300 mL) was added to a calcium hydroxide aqueous suspension (50.0 g of $Ca(OH)_2$ in 400 mL) containing iron chloride salts (12.7 g of $FeCl_2\cdot 4H_2O$ and 17.9 g of $FeCl_3\cdot 6H_2O$) as sources of Fe^{2+} and Fe^{3+} ions, respectively, at 40 °C and under constant stirring. After completion of the neutralization reaction, the medium was maintained in the same conditions for 1 h, and then matured 24 h at room temperature in static conditions. The precipitate was isolated from the medium by centrifugation, washed three times with deionized water by centrifugation, and freeze-dried. As for the HA compound, the powder sample obtained was sieved (<125 μm) and stored at −18 °C prior to use.

2.3. Physico-Chemical Characterizations. X-ray diffraction (XRD) and Fourier transform infrared (FTIR) spectroscopy were used to analyze the crystallography of the HA and FeHA substrates. XRD patterns were obtained on a D8 Advance diffractometer (Bruker, Karlsruhe, Germany) using Cu Kα radiation (λ = 1.54178 Å) and typically generated at 40 kV and 40 mA. Patterns were recorded in the 10−60° 2θ range with a step size of 0.02° and a counting time of 0.5 s. Sample crystallite sizes along the *c*-axis and along the perpendicular direction were estimated using Scherrer's formula[53] applied to the (002) and (310) reflections, respectively, at 2θ = 25.8° and 2θ = 39.7°. FTIR analyses were run on a Nicolet 5700 spectrometer (Thermo Fisher Scientific Inc., Waltham, MA) with a resolution of 2 cm^{-1} and accumulating 64 scans, in the 400−4000 cm^{-1} wavenumbers range, using the KBr pellet method.

Elemental titrations were carried out for checking the apatite compositions: calcium, phosphate, and iron contents were then determined by inductively coupled plasma optical emission spectrometry (ICP-OES) using a Liberty 200 spectrometer (Varian, Palo Alto, CA). For these analyses, 20 mg of sample was dissolved in 50 mL of HNO_3 solution 1 wt %. The carbonate content in the apatitic phases was carried out by coulometry using a CM 5014 coulometer with CM 5130 acidification unit (UIC Inc., Joliet, IL). All these chemical titrations were associated with a relative error of about 1%. The specific surface area (SSA_{BET}) of the samples was measured using a BELSORP mini II apparatus (Microtrac, Krefeld, Germany) via the BET method based on nitrogen adsorption.

Mean particle size (hydrodynamic diameters from dynamic light scattering, DLS) and overall surface charges (ζ-potential) of HA and FeHA samples were measured with a Zetasizer Nano ZS (Malvern, Worcestershire, UK). In these analyses, the nanoparticles (NPs) were suspended in 0.01 M HEPES buffer at pH 7.4 at a concentration of 0.1 mg/mL. Ten runs of 30 s were performed for each measurement, and four measurements were carried out for each sample. To evaluate the stability of apatite NPs in suspension, derived count rate (cps) were recorded continuously for 60 min. ζ-Potential was evaluated by laser Doppler velocimetry based on the concept of electrophoretic mobility, using disposable electrophoretic cells (Malvern, Worcestershire, UK). Twenty runs of 3 s were collected in each measurement.

Transmission electron microscopy (TEM) observations were realized on a Tecnai F20 microscope (FEI, Hillsboro, OR) equipped with a Schottky emitter and operating at 120 keV. The instrument was also equipped with an energy dispersive X-ray spectrometer (EDX) for X-ray microanalysis on selected areas. Sample preparation involved dispersion in isopropyl alcohol, treatment with ultrasounds and deposition of a few droplets of the slurry on holey-carbon foils supported on copper microgrids (300 mesh).

2.4. Adsorption Experiments. FA adsorption on the two nanocrystalline apatitic substrates, referred to here as HA and FeHA, was carried out at 37 °C using a constant solid-to-solution ratio corresponding to 20 mg of apatite immersed in 5 mL of FA solution, and for increasing FA concentrations (0−120 mg/mL). To facilitate FA dissolution and the preparation of increasingly concentrated FA solutions, the desired amount of FA powder was introduced in the vials followed by dropwise addition of sodium hydroxide until obtainment of a clear (yellow) solution indicating that FA had taken its folate form. Then, water and droplets of hydrochloric acid were added to finalize the desired volumes of solution and reach neutral pH. KCl was also added to reach a final concentration of 0.01 M in all vials used for adsorption tests to provide nearly constant ionic strength. During this immersion step, the vials were placed horizontally to ensure optimal interaction between the surface of the apatite substrates and the solution. After the contact time necessary to reach equilibrium (determined in a preliminary stage), the system was centrifuged (5000 rpm for 20 min) to separate the solid from the supernatant, and the latter was analyzed by UV (near visible) spectrophotometry at λ= 348 nm to quantify FA remaining in solution. Such spectrophotometry analyses were performed using a Cary Bio spectrophotometer (Varian, Palo Alto, CA) or alternatively a Shimadzu 8000 UV−vis spectrophotometer. The adsorbed amount was determined from the difference between the initial and supernatant concentrations. Some selected concentrations of MTX replacing FA were also used, when mentioned in the text, to check the similarity of adsorption behavior between FA and MTX, since MTX is an *antifolate* whose molecule highly resembles that of FA (Figure 1). In this case, MTX absorption was followed at λ = 372 nm.

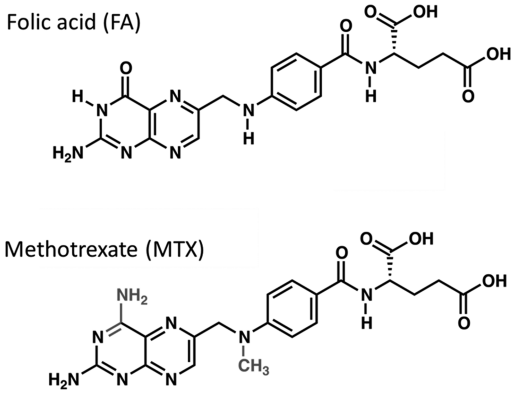

Figure 1. Molecular formulas of folic acid (FA) and its antifolate analogue methotrexate (MTX).

Confocal Raman microscopy (LabRAM HR800 microspectrometer, Horiba Jobin-Yvon) was also used for comparisons before and after FA adsorption. For these analyses, performed in the range 100−2000 cm^{-1}, the samples were exposed in backscattering mode to either a He/Ne laser (λ = 633 nm) with a power of 10 mW or with an Ar (diode) laser (λ = 532 nm) with a power of 17 mW, depending on FA fluorescence artifacts. The uncertainty on Raman shifts (<1 cm^{-1}) have been calibrated using a silicon standard at 520.7 cm^{-1}. An optical objective ×100 was used for all analyses, conferring to the system a lateral resolution of ∼0.8 μm and an axial resolution in the range 2.6−3.1 μm. In addition, to retain the integrity of the FA and FA/apatite samples, an opacity filter was used. The spectra reported in this work are the average of 3−5 spectral accumulations, where the exposure time was adapted to the sample. The amounts of phosphate ions present in the supernatant after adsorption were titrated by ICP-OES at λ = 214.914 nm (Ultima 2, Horoba Jobin Yvon).

FTIR, DLS, and ζ-potential analyses on the nanoparticles loaded with FA were carried out as reported above for the unfunctionalized apatites.

2.5. Release Experiments. FA release experiments from HA and FeHA (functionalized with maximum loading amount of FA) were carried out at 37 °C in the presence or absence of a pulsed electromagnetic field (PEMF). Investigations in the presence of PEMF were achieved placing the samples in the form of powder in a homemade device as previously reported,[54] consisting in a windowed PMMA tube carrying a well-plate containing the samples and two solenoids (i.e., Helmoltz coils, the planes of which were parallel). The generated magnetic field and induced electric field were respectively perpendicular and parallel to the samples, which were distant 5 cm from each solenoid plane, and a Biostim SPT pulse generator (Igea, Carpi, Italy) powered the solenoids. The electromagnetic stimulus had the following parameters: intensity of magnetic field 2.0 ± 0.2 mT, frequency of 75 ± 2 Hz, amplitude of induced electrical tension 5 ± 1 mV, pulse duration of 1.3 ms. For the release experiments, 5 mg of drug-apatite samples were immersed in 2.5 mL of HEPES at pH 7.4 (0.01 M HEPES, 0.01 M KCl), and samplings were drawn at selected time points over 6 days. After measurement of the temperature of the samples exposed to the PEMF, samples were then centrifuged (5000 rpm for 5 min) to separate the solid phase from the supernatant which was titrated for FA by UV spectrophotometry.

To complement this study, additional release (desorption) tests were also carried out, when mentioned in the text, at 37 °C in isotonic NaCl 0.9 wt %, with or without addition of potassium dihydrogen phosphate KH_2PO_4 (0.02 M).

2.6. In Vitro Evaluations. Human osteosarcoma cell line SAOS-2, obtained from the ATCC cell bank (Manassas, VA), was cultured in DMEM F12 (GIBCO), 10% FBS, and 100 U/mL penicillin/streptomycin. Cells were plated at a density of 5 × 10^3 cells/well in 96-well plates; 24 h after seeding, the samples were added to the culture and the cells were maintained in culture for 24, 48, and 72 h. HA and FeHA loaded with similar amount of MTX (101.8 and 99.6 mg of MTX on 1 g of HA and FeHA, respectively) were added to the culture at 5 and 50 μM concentration of attached MTX (Table SI1, Supporting Information). Moreover, the equivalent amounts of unfunctionalized HA and FeHA NPs used for each sample and free MTX were tested (Table SI1, Supporting Information). A group of cells only was used as control group. Cells were incubated under standard conditions (37 °C, 5% CO_2). All cell-handling procedures were performed in a sterile laminar flow hood.

The MTT reagent (3-(4,5-dimethylthiazol-2-yl)-2,5-diphenyltetrazolium bromide) was prepared at 5 mg/mL in 1× PBS. After experiments, the cell seeded in 96-well plates were incubated with the MTT reagent 1:10 for 2 h at 37 °C. After that, medium was collected and cells incubated with 200 μL of dimethyl sulfoxide for 15 min. In this assay, the metabolically active cells react with the tetrazolium salt in the MTT reagent to produce a formazan dye that can be observed at λ max of 570 nm, using a Multiskan FC Microplate Photometer (Thermo Scientific). This absorbance is directly proportional to the number of metabolically active cells. Mean values of absorbance were determined. The samples were analyzed in triplicate.

2.7. Subcutaneous Implantation in Mice. In order to check the overall biocompatibility of the HA and FeHA substrates, adult C57BL/6 mice (n = 3) between 10 and 12 weeks of age, weighing an average of 30 g were used for a subcutaneous implantation study. Protocol was submitted to the CREFRE ethics committee (CEEA122 US006/CREFRE) with approval number CEEA122:2015-18, in accordance with the European directive (DE 86/609/CEE; modified DE 2003/65/CE) for conducting animal experiments. Each animal received care in compliance to the Guide for The Care and Use of Laboratory Animals (Institute of Laboratory Animal Resources, National Research Councils; National Academy Press, revised 1996). They were fed with a standard laboratory diet and tap water ad libitum. All surgeries were performed under general anesthesia under sterile conditions. Anesthesia was induced by injection intraperitoneally (IP) of ketamine (75 mg/kg, Ketamine 500; Virbac France) and xylazine (5 mg/kg, Rompun; Bayer AG, Germany). Postoperative analgesia was achieved by injection of buprenorphine subcutaneously (0.05 mg/kg) every 12 h for 5 days.

The implementations were carried out subcutaneously (paravertebral, dorsal) after shaving the surgical site. Each mouse received two implants, one per side. Both HA and FeHA raw substrates were

evaluated here, after pelletizing by uniaxial pressing (HOUNSFIELD press series S, model H25KS, QMAT software) to obtain cylindrical pieces (diameter ~ 5 mm, height ~ 4.5 mm). 1% lidocaine was injected subcutaneously before incision. After implanting the surgical site was closed with sutures (Vicryl) to 4.0. A daily clinical follow-up was performed. Data regarding the general well-being of the animals and their weight were recorded throughout the duration of the experiment. After 3 weeks of implantation, the mice were euthanized with an intravenous overdose of sodium pentobarbital (150 mg/kg, Pentobarbital Sodique; CEVA Santé Animale, France) after administration of anesthesia (same protocol as previously described). A block resection, including surrounding tissues as well as the implants, was then performed in view of histological analyses (hematoxyline-eosine and Masson trichrome staining).

2.8. Statistical Analysis. Experiments were carried out in triplicate and results were expressed as mean and standard error of the mean (SEM). Analysis of cell viability was made by two-way analysis of variance (ANOVA), followed by Bonferroni's post hoc test. Statistical analyses were performed by the GraphPad Prism software (version 5.0), with statistical significance set at $p \leq 0.05$.

3. RESULTS AND DISCUSSION

3.1. Physico-Chemical Characteristics of HA and FeHA Powders. The samples have been characterized in a previous work.[30] The main characteristics are as follows. HA and FeHA exhibit XRD patterns with weakly defined peaks that can be indexed after hydroxyapatite crystallographic data (JCPDS card no. 09-432). The broad and poorly defined diffraction peaks are peculiar features of nanocrystalline bonelike apatites.[10] For the FeHA sample, the presence of maghemite Fe_2O_3 besides apatite was also pointed out by a peak at 35.4° corresponding to (311) diffraction line of this iron oxide phase (JCPDS card no. 03-0863), and its amount was evaluated to be 2.6 ± 0.2 wt %.[52] The iron oxide phase present in the FeHA sample was previously identified as maghemite also by extended X-ray absorption fine structure (EXAFS analysis) and Mössbauer spectroscopy.[44] FeHA exhibits a saturation magnetization of 4.00 ± 0.01 $Am^2\ kg^{-1}$, allowing hyperthermia properties with a temperature increase of about 40 °C in 60 s under an alternating magnetic field of 0.03 N $A^{-1}\ m^{-1}$ at a frequency of 293 kHz as previously shown.[43] Mean crystallite sizes were estimated by applying Scherrer's formula to lines (002) and (310), evidencing crystallites more elongated along the *c*-axis for FeHA compared to HA but similar perpendicular dimensions. The specific surface areas SSA_{BET} were respectively of 102 m^2/g for HA and 44 m^2/g for FeHA. TEM observation of HA pointed out elongated NPs (5−10 nm in width and 20−30 nm in length) while FeHA consisted in needle-like crystals, about 10−30 nm wide and 70−100 nm long, but composed of smaller aggregated NPs of about 5−10 nm in width and 10−20 nm in length. HA particles thus appeared less aggregated than FeHA, explaining their larger surface area.

ζ-Potential measurements revealed the globally negatively charged surfaces of the NPs, with values around −18 ± 1 mV at pH 7.4 for both HA and FeHA. Hydrodynamic diameters estimated from DLS measurements (around 74 nm for HA and 120 nm for FeHA) confirmed the nanometer size of the particles.

FTIR spectra of HA and FeHA disclosed the presence of typical vibration bands for bone-like apatite (i.e., PO_4^{3-} bands at ca. 560−603 (ν_4), 962 (ν_1), and 1000−1104 cm^{-1} (ν_3), and bands at 870 (ν_2), 1420 and 1470 cm^{-1} (ν_3) assignable to CO_3^{2-} vibrations essentially in B sites). Carbonation was found to be more intense for HA (3.0 ± 0.1 wt %) than FeHA (1.5 ± 0.1 wt %). The Ca/P ratios of HA (1.34 ± 0.03) and FeHA (1.41 ± 0.03) were in both cases lower than that of stoichiometric hydroxyapatite (1.67), evidencing the non-stoichiometry of these compounds as for bone apatite.

All the above physicochemical characteristics point out, for both compounds, their biomimetic apatitic features, resembling those of bone mineral.[5] They were then used as substrates to study FA (or MTX) sorption behaviors.

3.2. Adsorptive Behavior of FA (or MTX) on HA and FeHA Substrates. In a first stage, the kinetics of adsorption (at 37 °C) of FA on HA and FeHA have been explored. Results plotting the amount of FA adsorbed, Q_{ads} (in μmol/m^2), versus time for the same initial concentration, here 1 mg/mL or 2.27 mmol/L, are given in Figure 2. Despite slightly faster sorption on HA versus FeHA, rather similar kinetic trends may be observed in this low FA concentration domain, and the final adsorbed amounts reached in this case are of the same order. Mathematical modeling of the kinetics curves for both compounds has been undergone as previously described elsewhere,[24] and indicates that the best fits are obtained for the "order *n*" and Elovich models (with correlation coefficients R^2 close to each other, between 0.977 and 0.995), while other tested models as pseudo-first or pseudo-second order agree less well ($R^2 \ll 0.92$). This reminds the situation obtained for the adsorption of DOX on the same substrates;[30] in general, Elovich-like kinetics of adsorption are often encountered for the sorption of polyelectrolytes on heterogeneous surfaces. For the rest of the adsorption study, a contact time of 90 min was selected.

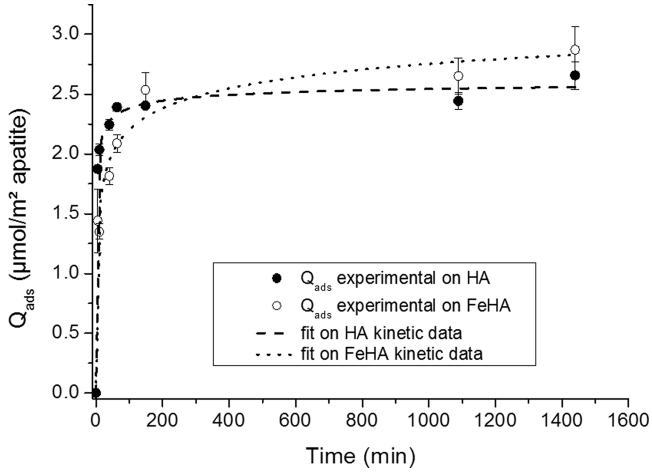

Figure 2. Kinetics of adsorption, at 37 °C, of folic acid (FA) on the two nanocrystalline apatite substrates HA and FeHA.

It can be noted that contact of the HA and FeHA substrates with the FA solutions led to a modification of their surface charge: for example, loading of the substrates with ca. 100 mg FA/g caused a shift of the ζ-potential of HA and FeHA toward less negative values (i.e., −9.0 ± 1.0 and −8.7 ± 1.0 mV, respectively, at pH 7.4). This shift can be tentatively explained by the interaction of FA with the surface of nanocrystalline apatite through the two carboxylate end-groups. In this case, the exposed positively charged amino group contributes to shift the surface charge of the nanoparticles toward more positive values. Consequently, the functionalized apatites were more aggregated, forming less stable suspensions than the bare ones with an increased mean hydrodynamic diameter of about

500 nm for both substrates analyzed by DLS. These observations are an indirect confirmation of the FA sorption event at the surface of the solids. More direct analyses arise from FTIR-ATR investigations allowing us to corroborate the effective functionalization of the particles with FA (Figure 3).

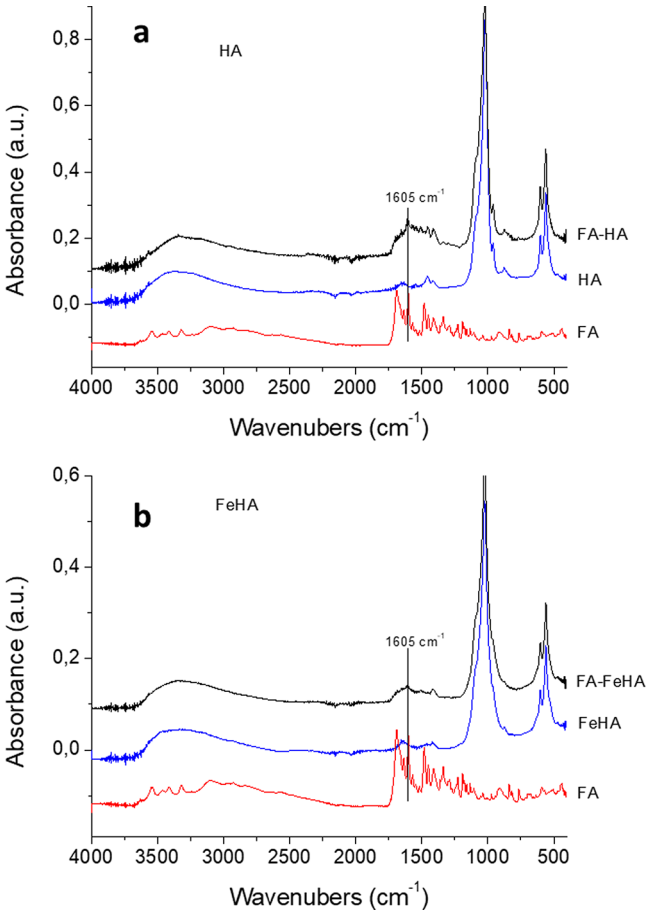

Figure 3. FTIR-ATR spectra before and after FA adsorption on HA (a) and FeHA (b).

These results point out spectral modifications of ATR features when FA is adsorbed on the apatitic substrates, with in particular the detection in the conjugates of a band at 1605 cm^{-1} characteristic of FA, in a similar way as was found by Cipreste et al.[50]

FA adsorption isotherms (at 37 °C) were then measured for both substrates by varying the FA concentration. Different sorption behaviors were obtained on HA and on FeHA, which are detailed in the following paragraphs. For information, the percentage of adsorption versus the initial amount incorporated is also accessible as Supporting Information (Figure SI1), pointing out a larger adsorption capacity for HA over FeHA.

FA sorption on HA pointed out the existence of two domains characterized by distinct features as shown on Figure 4a, with first a progressively saturating evolution of Q_{ads} (domain I) followed by a clear break in slope and steeper increase (domain II).

This general pattern suggests the existence of a secondary interaction mechanism detectable at high FA concentrations. Taking into account the ionic character of FA (in the form of folate ions in our experimental conditions), association with Ca^{2+} ions to form a calcium folate salt at increasing folate

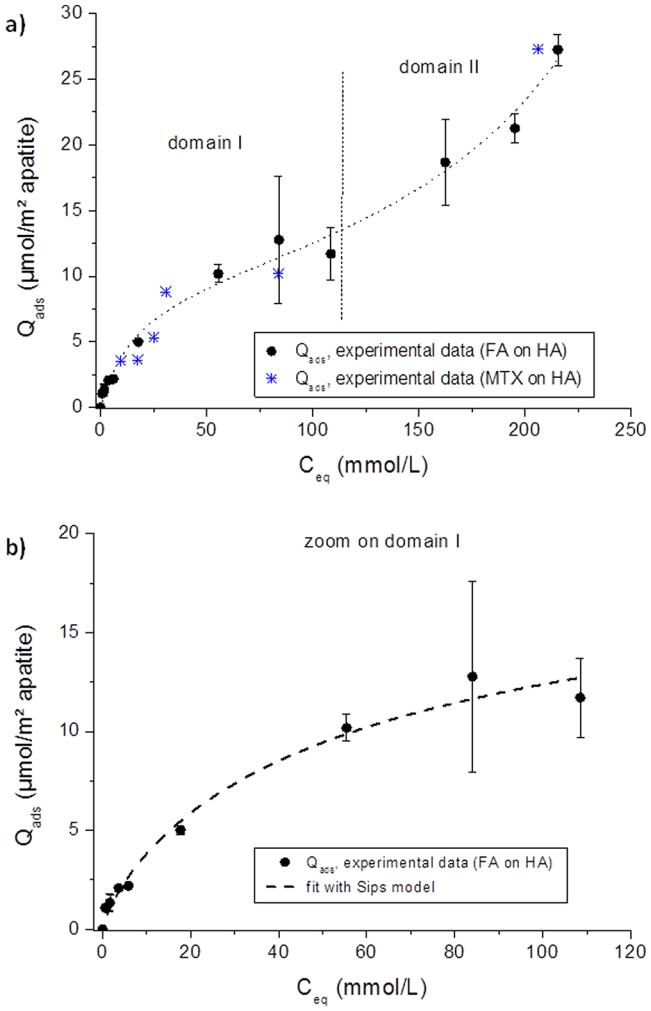

Figure 4. FA (or MTX) adsorption isotherm at 37 °C on nanocrystalline apatite sample HA: (a) general view and (b) zoom on domain I and fit of experimental data to the Sips model.

concentrations in solution appears as a likely scenario; calcium ions would originate from the partial dissolution of the HA surface following a right shift of the following equilibrium:

$$(\text{folate})^{2-} + Ca^{2+} \leftrightarrow Ca(\text{folate}) \quad (1)$$

Indeed, the formation of this secondary folate-containing salt would "artificially" consume FA (i.e., not in a way directly related to the adsorption process of FA on apatite), explaining the steeper increase noticed in domain II.

Focusing on domain I, that is to say for low to intermediate FA concentrations (typically up to 100 mmol/L), the isotherm resembles one of those often encountered with apatitic substrates (Figure 4). Although fitting to the Langmuir isotherm model leads to an acceptable R^2 coefficient (0.981), an even better accord is found with the Sips model ($R^2 \sim 0.984$), while the model of Freundlich leads to a poorer correspondence ($R^2 \sim 0.975$). Good fitting with the Sips model has already been observed for the adsorption onto biomimetic apatites of biomolecules like mono- or triphosphate nucleotides or drugs like tetracycline, and more recently DOX (on the same substrates as in the present study).[24,30,39−41] It points to a situation departing from the regular Langmuir theory which assumes in particular a lack of interaction between adjacent adsorbed species. In the present

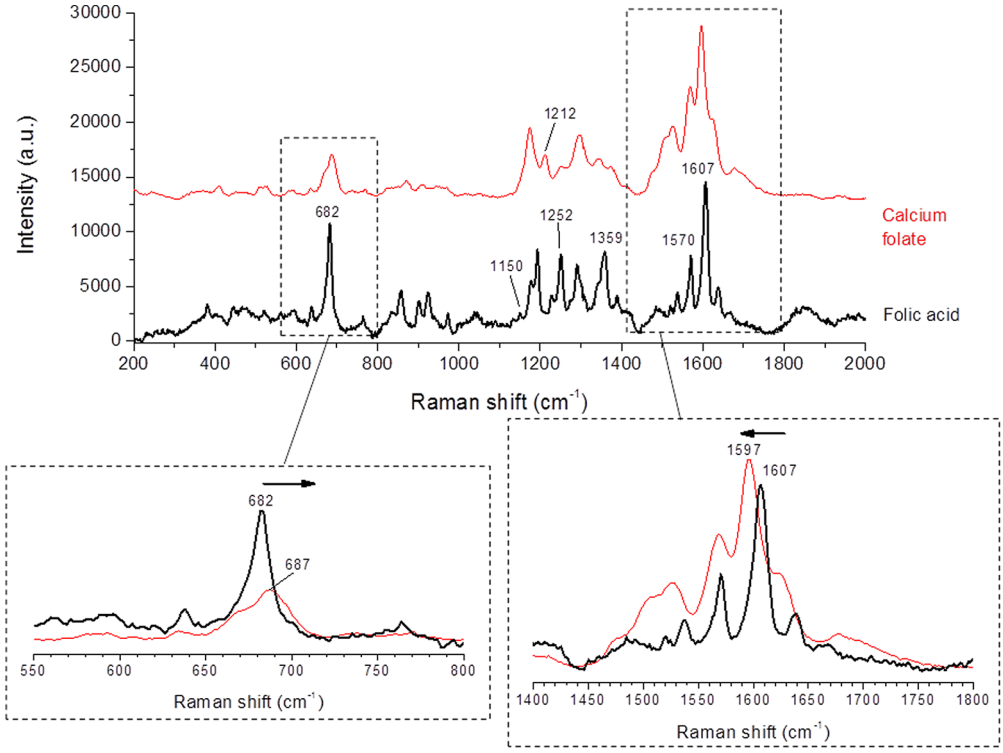

Figure 5. Raman spectra for pure FA and precipitated calcium folate.

case, the following Sips parameters are found: $m \sim 0.81 \pm 0.14$, $K \sim 0.0342_5 \pm 0.080_5$ (for C_{eq} expressed in mmol/L), and $Q_{max} \sim 21.25 \pm 7.13$ μmol FA/m^2 apatite. The value of the exponent m lower than 1 suggests a situation where negative cooperativity between adjacent sorbed molecules may occur, as was also inferred for the adsorption of adenosine triphosphate (ATP) on nanocrystalline apatite.[39] The value $Q_{max} \sim 21.25 \pm 7.13$ μmol FA/m^2 evaluated here from Sips model has not been experimentally reached within domain I (up to $Q_{ads} \sim 12$ μmol/m^2), since beyond a concentration of about 120 mmol/L the second phenomenon related to calcium folate formation gets superimposed. However, even the value of 12 μmol/m^2 deserves attention as it is still larger than usually found for the sorption of (bio)molecules on apatite (see comparative discussion in ref 30). For DOX adsorption, a surprisingly high adsorbed amount had been reached too on these two substrates[30] (experimentally noticed up to ~8 μmol/m^2 on HA and ~18 μmol/m^2 on FeHA); however, in that case, the involvement of $\pi-\pi$ stacking between adjacent DOX molecules, which exhibit a very characteristic planar conformation, came into play.[30] In contrast, for FA π stacking cannot reasonably be claimed (which would require a large planar molecular domain). On the other hand, examination of the full FA adsorption isotherm (Figure 4) has led us in the above discussion to conjecture the formation of a secondary calcium folate salt at least for high FA concentrations. Considering the high values of Q_{ads} reached here, up to ~12 μmol/m^2 in domain I, the formation of this secondary calcium folate salt *even at lower concentrations* also appears plausible during the FA/apatite immersion to explain our experimental observations.

To investigate further this point, Raman spectra have been acquired on FA alone and on precipitated calcium folate (obtained by mixing FA with calcium chloride at room temperature followed by filtering, washing and drying) (Figure 5). Raman spectra of FA adsorbed on HA corresponding to FA adsorbed amounts of 9.7 μmol/m^2 (within domain I of the adsorption isotherm) and 24.4 μmol/m^2 (within domain II) are also reported (Figure 6). Most of the vibrational bands from the Raman spectrum of pure FA are in concordance with the literature,[55,56] especially with bands in the range 600−1700 cm^{-1}. The most intense contribution is located at 1607 cm^{-1} and can be related to the stretching vibration of NH from the pteridine ring of FA. Other medium intensity Raman bands are observed at 1570 cm^{-1}, 1359 cm^{-1}, between 1150 and 1252 cm^{-1}, and at 682 cm^{-1} which are attributed to the asymmetric C═N vibration, the CH rocking vibration from the benzoic acid moiety, the rocking vibration of C═N, and the asymmetric vibration of C═C, respectively. Significant shifts (up to about 10 cm^{-1}) were observed when comparing pure FA to the calcium folate salt, especially in the OH domain (around 682 cm^{-1}) toward higher wavenumbers (around 687 cm^{-1}) and in the domain of NH aromatic ring chain vibrations (around 1607 cm^{-1}) toward lower wavenumbers (1597 cm^{-1}). Moreover a broadening of the bands and the presence of an additive contribution around 1212 cm^{-1} can be observed on the spectrum of the calcium salt.

Despite the fluorescence of FA, Raman spectra of HA powders after adsorption showed (Figure 6), as expected, the presence of the apatitic phase, especially detectable by its $\nu_1(PO_4)$ characteristic band[57,58] at 962 cm^{-1}. Several other lines, e.g., close to 682 cm^{-1} (as in pure FA) corresponding to aromatic ring chain vibrations and at an intermediate position between 1597 and 1607 cm^{-1}, testify to the presence of FA. These observations, along with a shift in the domain of the aromatic ring chain vibrations and the concomitant presence of the band around 1215 cm^{-1}, are coherent with the adsorption isotherm data suggesting the formation of a calcium folate salt besides FA adsorbed on HA (for both domains I and II of the adsorption isotherm).

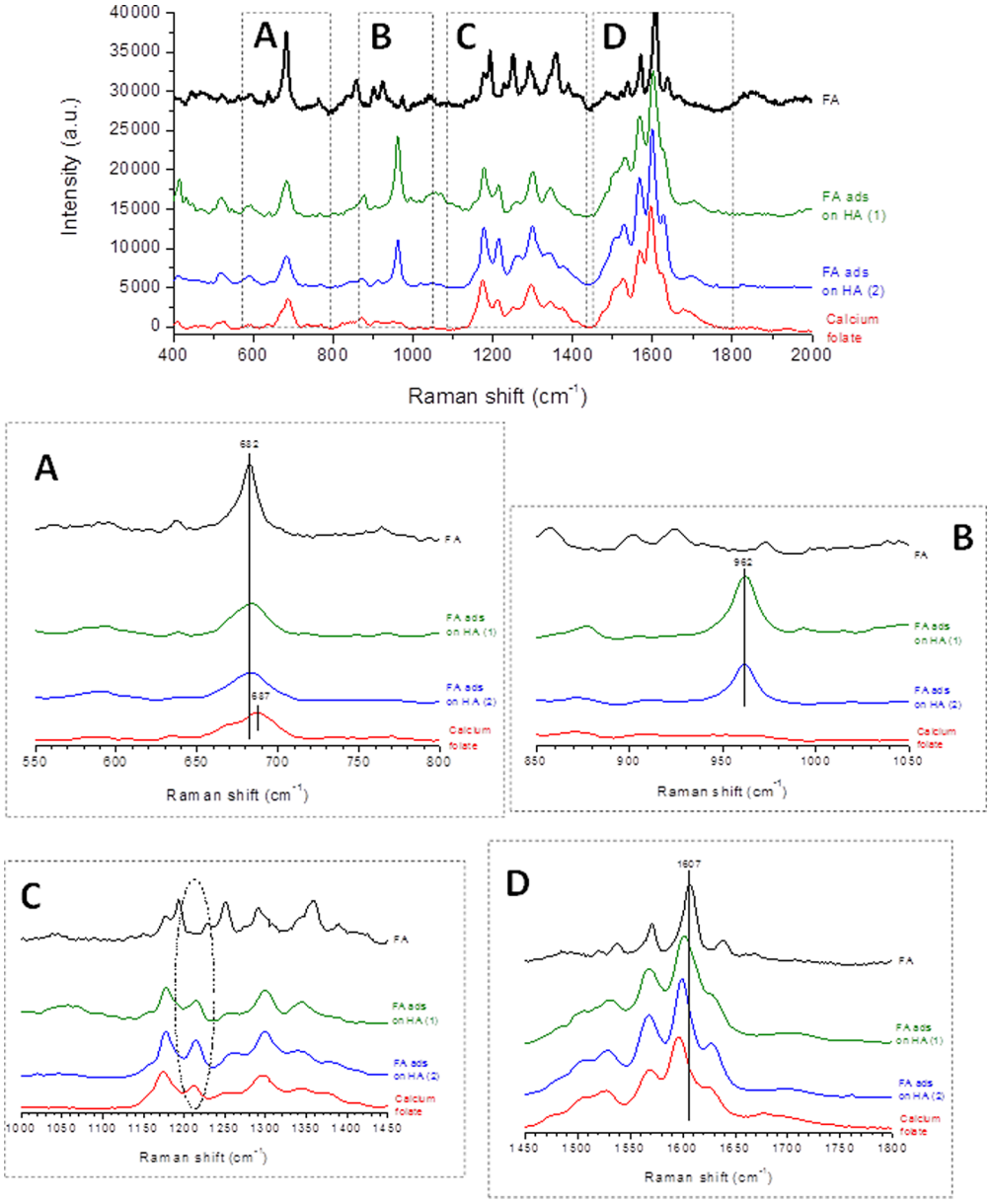

Figure 6. Raman spectra for FA adsorbed on HA as well as pure FA and precipitated calcium folate. Adsorption points (1) and (2), respectively, correspond to FA adsorbed amounts of 9.7 μmol/m^2 (domain I) and 24.4 μmol/m^2 (domain II)

The conjunction of all the results above (general shape of adsorption isotherm, high Q_{ads} values, Raman signature at 1213 cm^{-1}) supports the hypothesis of a secondary calcium folate precipitation besides the primary FA adsorption onto HA. In this context, for high folate concentrations in solution, an increased consumption of Ca^{2+} ions is expected so as to form the calcium folate salt (evolution from left to right on eq 1). In turn, this effect can favor the partial dissolution of apatite (in order to preserve the solubility product), providing additional calcium and phosphate ions to the solution. It may thus be interesting to complement this study by the analysis of ionic concentrations in the supernatants after adsorption process. The case of calcium ions is however delicate as calcium is both involved in the consumption with folate and in the release from apatite; in contrast, it is appropriate to follow the evolution of phosphates in solution as these ions will only be linked to apatite dissolution. This follow-up has been done by ICP-OES titrations of phosphorus, for several points over the whole C_{eq} range of the isotherm presented in Figure 4a. Although phosphate concentrations [P] remained rather low, an increasing trend in the [P] = $f(Q_{ads})$ and the [P] = $f(C_{eq})$ plots can be noticed (Figure SI2, Supporting Information), roughly between 0.8 and 1.6 mg/L. This trend, evidencing an increased HA dissolution upon adsorption, was indeed expected on the basis of the above discussion.

This sorption overview now makes it possible to predict, from a given FA concentration, which amount will be associated with the solid phase and with which mechanism of interactions. This is intended to prove helpful, for example, in view of preparing apatite-based nanoparticles for applications in the field of oncology using FA as cancer cell targeting agent. Moreover, a similar behavior may also be expected for the adsorption of parent molecules such as antifolates like methotrexate (MTX). In this regard, some selected adsorption points for MTX on HA have also been recorded in this work (corresponding to concentrations of MTX ranging throughout

the adsorption isotherm, relevant for therapy) and they have been added in Figure 4a. As expected, a reasonably good accord may be indeed found with the FA isotherm, thus also opening therapeutic perspectives.

In a parallel way, the same adsorption study as above has been carried out on the FeHA iron-containing nanocrystalline apatitic substrate. The corresponding FA adsorption isotherm (at 37 °C) is reported on Figure 7. In this case, despite a

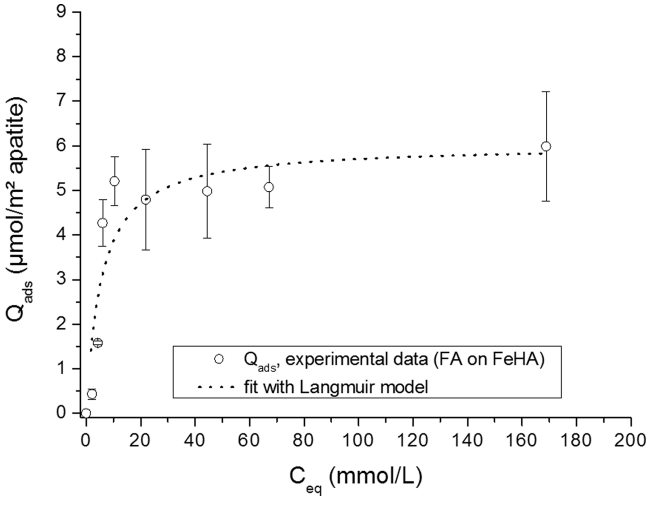

Figure 7. FA adsorption isotherm at 37 °C on iron-doped nanocrystalline apatite sample FeHA, and fit with the Langmuir model.

cloudiness in the data points, a simpler $Q_{ads} = f(C_{eq})$ curve shape was identified when compared to HA, with a progressive rather monotonous increase of Q_{ads} until stabilization.

Mathematical modeling of the plot showed that it could be described—although not perfectly due to non-negligible error bars, with the Langmuir model in a first approximation (equivalent to Sips model with $m = 1$, leading to $R^2 \sim 0.855$) as opposed to Freundlich ($R^2 \sim 0.5941$) or Temkin ($R^2 \sim 0.8346$). The cloudiness of data points for FeHA may reasonably be related to the heterogeneous nature of this compound, associating apatite particles and maghemite clusters. Nevertheless, in the case of FeHA a Langmuir-like general form of the isotherm is noticed, without a clear change in slope for increasing C_{eq}, unlike for HA. This indicates that the formation of a secondary salt such as calcium folate, even if present, cannot be directly detected. This may be related to the physicochemical features of the FeHA substrate which exhibits a lower surface area as well as a lower carbonation and a composition closer to stoichiometry (larger Ca/P ratio) compared to HA which is more carbonated, presents a larger surface area and a composition farther from stoichiometry. This implies that FeHA has a lower solubility compared to H (the closer from stoichiometry, the more thermodynamically stable (less soluble) as shown by a previous thermodynamic dedicated study on biomimetic apatites[59]). Since the formation of a calcium folate secondary salt would necessitate (partial) apatite dissolution to provide Ca^{2+} ions, it is not surprising that this phenomenon is less favored for FeHA, thus not provoking a major perturbation on the adsorption isotherm. Although this remark does not necessarily imply the absence of calcium folate salt, it is expected to have less effect on the overall adsorption process. The maximal FA adsorbable amount Q_m on FeHA is evaluated to be 6.02 ± 0.66 µmol/m² from the Langmuir fit. This value is, as expected by the less prominent role of calcium folate, lower than that recorded on the HA substrate in domain I (see Figure 4) and is likely explainable by the affinity of the two nearly adjacent carboxylic end-groups exhibited by FA for apatite. The Langmuir constant K was here evaluated from the mathematical fit to be $K \sim 0.1792 \pm 0.079$ (for C_{eq} expressed in mmol/L). This value of the so-called "affinity constant" is significantly greater than the one obtained above for HA ($K \sim 0.03425 \pm 0.0805$), suggesting a greater affinity of FA on FeHA than on HA. This difference is probably assignable to the different physicochemical characteristics of the two substrates: the less mature HA apatite exhibiting a larger surface reactivity (and a greater potential for postmaturation when reimmersed in solution) than the more mature FeHA.

The concentration of phosphate ions present in the supernatants upon adsorption was also measured, as previously done for the HA substrate. In this case (Figure SI3, Supporting Information), no clear trend in the [P] plot versus Q_{ads} (or C_{eq}) was detectable, with [P] remaining close to 0.8 mmol/L in all cases. These findings agree well with the above conclusions suggesting the less significant role of calcium folate in the adsorption of FA on FeHA in these experimental conditions.

Raman spectra of FeHA powders were also tentatively recorded. However, in this case portions rich in iron oxide led to broad bands in the range 1150−1400 cm^{-1} which is a specific domain of interest to examine the presence of calcium folate salt (Figure SI4, Supporting Information). Therefore, the Raman analysis of FeHA was not pursued for following the adsorption process. It may only be noted that the most intense band attributed to the $\nu_1(PO_4)$ mode of the apatite phase was detected in FeHA substrate with a maximum at 958 cm^{-1}, which appears shifted in comparison to Fe-free apatite, as shown in Figure SI5 (Supporting Information). This shift can be attributed to the insertion of Fe ions in the apatitic structure.

In conclusion of this section, the sorption of FA (or MTX) on HA or FeHA has been investigated from a qualitative and quantitative viewpoint. Adsorption appears to be guided by the presence of the two carboxylate end-groups on the FA (or MTX) molecule conferring some affinity for the surface of nanocrystalline apatites, but the sorption process is probably essentially of physical rather than chemical nature. The affinity constant found on FeHA is greater than on HA. In addition, the formation of a secondary calcium folate salt besides FA sorption was evidenced especially on HA (which exhibits a greater solubility and a larger surface area than FeHA). The analysis of some MTX adsorption data points, relevant from a medical viewpoint, showed that they fell close to those of FA, thus allowing us to extrapolate the quantitative data from FA (easily handled, nontoxic molecule), to MTX (chemotherapeutic, toxic drug).

3.3. Release Data. Release experiments were carried out over 6 days, in HEPES at 37 °C and pH 7.4. Taking into account the magnetization of FeHA and its potential role on desorption activation as observed for DOX,[30] release experiments were performed both in the presence and in the absence of external pulsed electromagnetic field (denoted PEMF). Tests were carried out from samples preadsorbed with FA using rather close initial loadings selected as follows: 136.65 mg/g (corresponding to 3.04 µmol/m²) for HA and 100.20

mg/g (corresponding to 5.16 μmol/m^2) for FeHA. These values were chosen for being close to each other while limiting also the effect of calcium folate secondary salt in the case of HA. Our results indicated (Figure 8) that the application of an

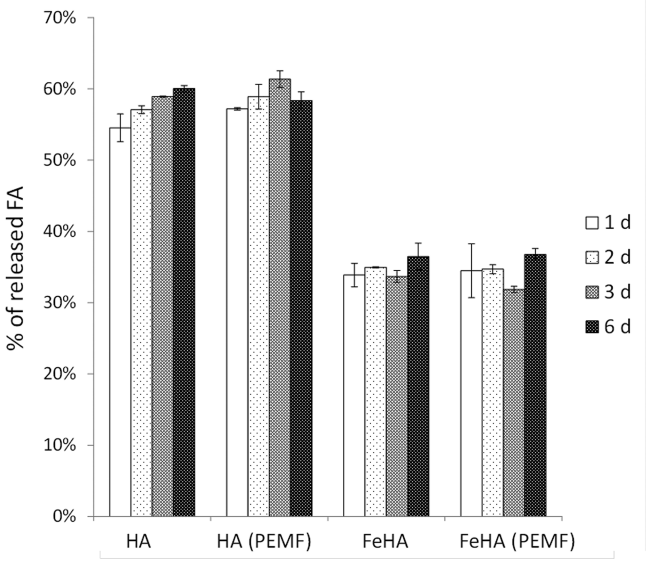

Figure 8. Kinetic of FA release from HA and FeHA from 1 to 6 days, in the presence or absence of PEMF.

external magnetic field did not have a detectable effect on FA release. FA release from these apatitic substrates indeed does not appear to be activated by additional vibratory motions within the FeHA sample unlike previously revealed for DOX.[30] In the latter case, interaction between DOX and FeHA involved multimolecular assemblies (dimers, trimers or even much larger polymolecular units) on the nanoparticles surface,[30] forming several layers of DOX molecules interacting among them by $\pi-\pi$ stacking thanks to their coplanar aromatic molecular domains. In that case, when the FeHA-DOX samples were exposed to a low-frequency PEMF, the mechanical shacking of FeHA allowed the enhancement of drug release at long time points (i.e., 3 and 6 days) since the bonding among multimolecular assemblies as well as between the drug and nanoparticles was weakened by the continuous pulsed stimulation.[30] In the case of FeHA-FA the same phenomenon was not observed as no significant increase of FA release was observed after 3 days. This might be related to the fact that differently to DOX, the FA molecule cannot undergo relatively weak $\pi-\pi$ stacking interactions (absence of a large planar molecular domain).

Generally speaking, the desorption of FA from both the carriers was rather fast. In fact, release experiments at early time points (Figure SI6) revealed that after the first 10 min around 33 and 40 wt % FA were desorbed from FeHA and HA, respectively, and after 30 min these values grew up to around 35 and 50 wt %. In both cases, the plateau was reached after 60 min, and corresponded to 38 and 55 wt % released FA for FeHA and HA, respectively.

In all the cases, the amount of FA released was quite high, and larger for HA (in the range 55−60 wt %) than for FeHA (35−40 wt %). This difference is in perfect agreement with our above results on the sorption of FA on each substrate, which pointed out a significantly larger affinity of FA for FeHA than on HA. However, the high released amounts observed by simple reimmersion of the samples in HEPES buffer solutions show that FA affinity for the surface of such apatites remains rather low. Therefore, an eventual ion release from the apatite surface simultaneous with the adsorption process itself (e.g., phosphate release from the apatite surface for "anchoring" the adsorbed molecule) as already found for bisphosphonates[28] can be ruled out here. This conclusion confirms that FA sorption can most probably be described as a physisorption phenomenon.

Additional experiments were focused on the desorption of FA from the two substrates by immersion at 37 °C in NaCl 0.9 wt %, in the absence or presence of phosphate ions in the form of KH_2PO_4 0.02 M. Figure SI7 (Supporting Information) reports the results obtained for similar initial FA loading rates of ca. 100 mg/g. As can be seen, desorbed amounts (in wt %) are again larger from HA than from FeHA for any given condition, which is in accordance with the above results pointing to greater affinity of FA for FeHA than for HA. It can also be noted that addition of phosphate ions in the medium tends to favor FA desorption in the case of HA while it remains almost unchanged for FeHA. Since the adsorption of FA on HA was shown to be accompanied by the secondary formation of calcium folate salt, the effect of an increase of phosphate concentration in the medium can be explained by the displacement of chemical equilibria: increasing phosphate concentration will promote apatite formation versus its dissolution, thus favoring in turn the dissolution of the calcium folate salt in order to provide the necessary Ca^{2+} ions (eq 1 favored from right to left).

These desorption tests thus point out the possibility for adsorbed FA (or MTX which was shown above to have a similar adsorption behavior) to be desorbed upon reimmersion, which may be exploited to convey antitumor effect to such compounds. This can be especially expected in the case of HA where the release is shown to be more significant.

3.4. In Vitro Tests. Assessment of osteosarcoma cells viability grown in the presence of 5 and 50 μM MTX, either free or loaded onto HA and FeHA, as well as with equivalent amounts of unfunctionalized nanoparticles was carried out by quantification of metabolically active cells by the use of the MTT assay.

Results indicated that the MTX loaded onto HA, and supplied to the cells at 50 μM of MTX, was able to exert a cytotoxic activity on SAOS-2 cells (Figure 9a). As reported, HA-MTX 50 μM showed reduction of cell viability compared to the cells only sample, with statistic difference at 72 h of culture, $p \leq 0.0001$. Moreover, HA-MTX 50 μM significantly reduced cell viability compared to both the tested concentrations of the unfunctionalized HA (HA Ct1 and HA Ct2 with $p \leq 0.05$ and $p \leq 0.0001$, respectively). In contrast to HA, no significant differences were observed in cell viability after treatment with FeHA loaded with MTX at all the time points (Figure 9b).

In order to obtain anticancer efficacy, MTX molecules must be internalized into the cell with high concentration.[60] However, MTX molecules themselves cannot easily permeate through the cell membrane due to the repulsive interaction between anionic MTX and negatively charged cell membrane giving rise to a low drug efficacy.[61] Moreover it is well reported that MTX itself needs a lag-time to be effective because of its very short half-life that results in a decrease of its concentration in the initial period.[60] Accordingly, our results indicate that only the highest concentration of MTX tested is cytotoxic to

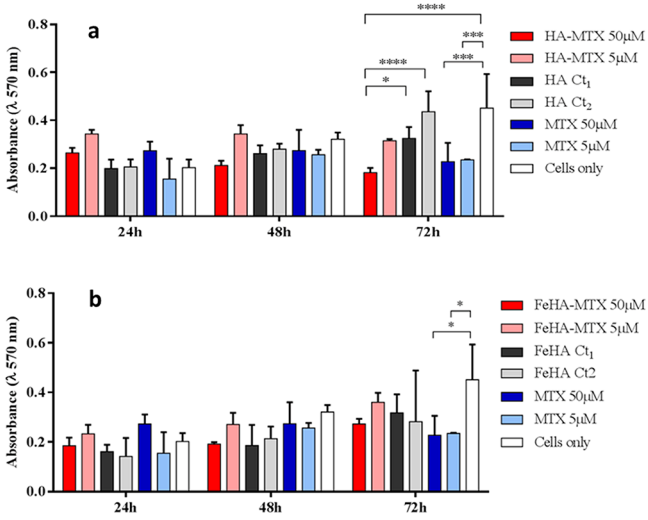

Figure 9. Analysis of SAOS-2 cell line viability by the MTT assay, after 24, 48, and 72 h of culture with 5 and 50 μM MTX either free or loaded on (a) HA and (b) FeHA, as well as with equivalent amounts of unfunctionalized (a) HA and (b) FeHA. The sample with only cells was used as the control. The graph shows the average and standard error of three replicates; statistical significant differences among the samples are indicated in the graphs: $*p \leq 0.05$, $***p \leq 0.001$, and $****p \leq 0.0001$.

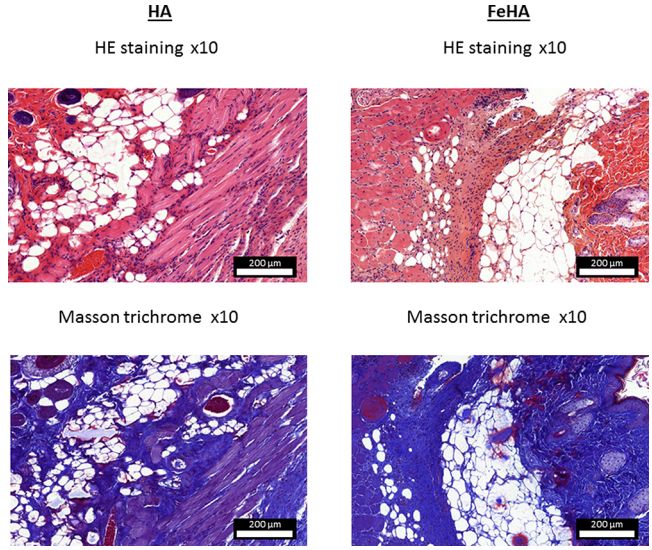

Figure 10. Histological data (hematoxylin/eosin (HE) and Masson trichrome stainings) after subcutaneous implantation (3 weeks) in mice of HA and FeHA substrates.

the SAOS-2 cell type, and that this cytotoxicity shows up significantly after 72 h of culture.

Previously published works have reported that MTX loaded on layered double hydroxides[60,61] and on mesoporous zinc-hydroxyapatite functionalized with Pluronic F127 possess higher antitumor efficacy on SAOS-2 respect to free MTX.[62] Authors explained this behavior with the fact that MTX can penetrate the tumor cell membrane without any early decomposition through a nanostructure-mediated internalization.

Overall, our data show that MTX supported on HA at the highest concentration tested exerts cytotoxic effect. This is however not observed with FeHA. The difference in cytotoxicity between HA-MTX and FeHA-MTX can be due to the higher MTX release from HA compared to FeHA and not to different internalization processes that should be similar as showed in our previous work with DOX.[30]

3.5. Substrate Biocompatibility Analysis via Subcutaneous Implantation in Mice. The materials studied in this work could be envisioned for drug delivery, e.g., in bone tumor sites, either in the form of slurries or as scaffolds. In order to evaluate in an in vivo situation the general biocompatibility of HA and FeHA, subcutaneous (intervertebral) implantations were realized in mice. The samples were pelletized by uniaxial pressing prior to implantation. After implantation (3 weeks), a block resection of the implanted areas was performed for histological analyses. The HA implanted samples had disappeared almost completely while FeHA was still present. These findings point out the more resorbable property of the HA sample as compared to FeHA, which is in perfect agreement with the above results suggesting a larger solubility of HA. On resection, the remaining biomaterials separated easily from the skin. Analysis of the skin tissue immediately in contact with the materials was subjected to histomorphological analyses. For FeHA, histology data indicated (Figure 10) that the skin exhibited close to normal aspect. In the hypodermis, a moderately abundant inflammatory infiltrate was detected, associated with some polynuclear cells. Only rare giant multinuclear cells were observed. Also, a fibroblastic reaction and a loose collagen deposit were noticed. These findings represent a natural healing process and do not show high inflammatory or foreign-body reaction, evidencing a good biocompatibility of the implanted material. For HA, similar observations were made, only with a more abundant infiltrate, often gathered in islands, and a more important fibroblastic reaction associated with rather dense collagenic deposits in the dermis and hypodermis. These observations (see also Figure SI8, Supporting Information) are characteristic of the healing process, especially activated due to the higher resorbability of HA. Again, the results evidence a good biocompatibility of the material and the absence of a high foreign-body reaction.

4. CONCLUSIONS

This study explored the interaction between FA or its chemotherapeutic derivative, MTX, and bioinspired nanocrystalline apatite substrates exhibiting, or not, superparamagnetic properties. The sorption behaviors have been investigated and explained on the basis of mathematical modeling of experimental data. The two nanocrystalline apatite-based compounds can be associated with FA/MTX in quantitative amounts; however, a greater affinity of these molecules for FeHA has been observed compared to HA. Consequently, a larger propensity for drug release is found for HA which proved to be effective on SAOS-2 sarcoma osteogenic cells. The biocompatibility of the two substrates was also evidenced by way of subcutaneous implantations in mice. By their versatility in terms of drug affinities and release behaviors, but also their nanocrystalline biomimetic character, these two bioinspired apatite substrates are promising in the field of oncology, whether using FA as cancer cell targeting agent and/or using MTX to treat bone cancers.

■ ASSOCIATED CONTENT

Supporting Information

The Supporting Information is available free of charge on the ACS Publications website at DOI: 10.1021/acs.langmuir.8b02602.

Evolution of FA loading percentage; Evolution of phosphate concentration; Raman spectra; FA desorption kinetics; desorption tests; experimental conditions for in vitro tests (PDF)

■ AUTHOR INFORMATION

Corresponding Authors

*E-mail: christophe.drouet@cirimat.fr. Tel: +33(0)534323411.
*E-mail: stephanie.sarda@iut-tlse3.fr. Tel: +33(0)534323416.
*E-mail: michele.iafisco@istec.cnr.it. Tel: +39 0546699730.

ORCID

Alessio Adamiano: 0000-0002-2077-0411
Christophe Drouet: 0000-0002-8471-8719

Present Address

[‖]P.P.-M.: University of Limoges, CNRS, IRCER UMR 7315, CEC, 12 Rue Atlantis, 87068 Limoges Cedex, France.

Notes

The authors declare no competing financial interest.

■ ACKNOWLEDGMENTS

We acknowledge support from the French Campus France association (Hubert-Curien "Galilée" program, project #28285UB) and from the Università Italo-Francese (Programma Galileo 2012/2013), as well as from the Italian Ministry for Education, University and Research (MIUR) in the framework of the Flagship Project NanoMax (PNR 201-2013). The Biostim SPT pulse generator was kindly provided by IGEA (Carpi, Italy). The authors also thank Prof. T. Al-Saati and Dr. F. Capilla for support in the histology lab work performed at CPTP, University Hospital of Toulouse.

■ REFERENCES

(1) Wopenka, B.; Pasteris, J. D. A mineralogical perspective on the apatite in bone. *Mater. Sci. Eng., C* **2005**, *25* (2), 131−143.
(2) Daculsi, G.; Laboux, O.; Malard, O.; Weiss, P. Current state of the art of biphasic calcium phosphate bioceramics. *J. Mater. Sci.: Mater. Med.* **2003**, *14* (3), 195−200.
(3) Tampieri, A.; Celotti, G.; Landi, E.; Sandri, M.; Roveri, N.; Falini, G. Biologically inspired synthesis of bone-like composite: self-assembled collagen fibers/hydroxyapatite nanocrystals. *J. Biomed. Mater. Res.* **2003**, *67* (2), 618−25.
(4) Rey, C.; Combes, C.; Drouet, C.; Gimcher, M. In *Bone mineral: update on chemical composition and structure*; 3rd Meeting on Bone Quality, 2009; 2009; pp 1013−1021.
(5) Gomez-Morales, J.; Iafisco, M.; Delgado-Lopez, J. M.; Sarda, S.; Drouet, C. Progress on the preparation of nanocrystalline apatites and surface characterization: Overview of fundamental and applied aspects. *Prog. Cryst. Growth Charact. Mater.* **2013**, *59* (1), 1−46.
(6) Rey, C.; Shimizu, M.; Collins, B.; Glimcher, M. J. Resolution-enhanced Fourier-transform infrared-spectroscopy study of the environment of phosphate ions in the early deposits of a solid-phase of calcium-phosphate in bone and enamel, and their evolution with age 0.1. Investigations in the v4 PO4 domain. *Calcif. Tissue Int.* **1990**, *46* (6), 384−394.
(7) Rey, C.; Lian, J.; Grynpas, M.; Shapiro, F.; Zylberberg, L.; Glimcher, M. J. Non-apatitic environments in bone mineral: FT-IR detection, biological properties and changes in several disease states. *Connect. Tissue Res.* **1989**, *21* (1−4), 267−73.
(8) Lopez-Macipe, A.; Gomez-Morales, J.; Rodriguez-Clemente, R. Nanosized hydroxyapatite precipitation from homogeneous calcium/citrate/phosphate solutions using microwave and conventional heating. *Adv. Mater.* **1998**, *10* (1), 49−53.
(9) Cuneyt Tas, A. Synthesis of biomimetic Ca-hydroxyapatite powders at 37 degrees C in synthetic body fluids. *Biomaterials* **2000**, *21* (14), 1429−38.
(10) Vandecandelaere, N.; Rey, C.; Drouet, C. Biomimetic apatite-based biomaterials: on the critical impact of synthesis and post-synthesis parameters. *J. Mater. Sci.: Mater. Med.* **2012**, *23* (11), 2593−2606.
(11) Wang, J.; Shaw, L. L. Morphology-Enhanced Low-Temperature Sintering of Nanocrystalline Hydroxyapatite. *Adv. Mater.* **2007**, *19* (17), 2364−2369.
(12) Ganesan, K.; Epple, M. Calcium phosphate nanoparticles as nuclei for the preparation of colloidal calcium phytate. *New J. Chem.* **2008**, *32* (8), 1326−1330.
(13) Zhang, Y.; Lu, J. A simple method to tailor spherical nanocrystal hydroxyapatite at low temperature. *J. Nanopart. Res.* **2007**, *9* (4), 589−594.
(14) Guo, X. Y.; Gough, J. E.; Xiao, P.; Liu, J.; Shen, Z. J. Fabrication of nanostructured hydroxyapatite and analysis of human osteoblastic cellular response. *J. Biomed. Mater. Res., Part A* **2007**, *82A* (4), 1022−1032.
(15) Chaudhry, A. A.; Haque, S.; Kellici, S.; Boldrin, P.; Rehman, I.; Khalid, F. A.; Darr, J. A. Instant nano-hydroxyapatite: a continuous and rapid hydrothermal synthesis. *Chem. Commun.* **2006**, No. 21, 2286−2288.
(16) Ashok, M.; Kalkura, S. N.; Sundaram, N. M.; Arivuoli, D. Growth and characterization of hydroxyapatite crystals by hydrothermal method. *J. Mater. Sci.: Mater. Med.* **2007**, *18* (5), 895−898.
(17) Ben-Nissan, B.; Choi, A. H. Sol-gel production of bioactive nanocoatings for medical applications. Part 1: an introduction. *Nanomedicine (London, U. K.)* **2006**, *1* (3), 311−9.
(18) Sun, G. M.; Zhang, X. Z.; Chu, C. C. Formulation and characterization of chitosan-based hydrogel films having both temperature and pH sensitivity. *J. Mater. Sci.: Mater. Med.* **2007**, *18* (8), 1563−1577.
(19) Chai, C. S.; Ben-Nissan, B. Bioactive nanocrystalline sol-gel hydroxyapatite coatings. *J. Mater. Sci.: Mater. Med.* **1999**, *10* (8), 465−469.
(20) Iafisco, M.; Delgado-Lopez, J. M.; Gomez-Morales, J.; Hernandez-Hernandez, M. A.; Rodriguez-Ruiz, I.; Roveri, N. Formation of calcium phosphates by vapour diffusion in highly concentrated ionic micro-droplets. *Cryst. Res. Technol.* **2011**, *46* (8), 841−846.
(21) Nassif, N.; Martineau, F.; Syzgantseva, O.; Gobeaux, F.; Willinger, M.; Coradin, T.; Cassaignon, S.; Azais, T.; Giraud-Guille, M. M. In Vivo Inspired Conditions to Synthesize Biomimetic Hydroxyapatite. *Chem. Mater.* **2010**, *22* (12), 3653−3663.
(22) Phillips, M. J.; Darr, J. A.; Luklinska, Z. B.; Rehman, I. Synthesis and characterization of nano-biomaterials with potential osteological applications. *J. Mater. Sci.: Mater. Med.* **2003**, *14* (10), 875−882.
(23) Roveri, N.; Palazzo, B.; Iafisco, M. The role of biomimetism in developing nanostructured inorganic matrices for drug delivery. *Expert Opin. Drug Delivery* **2008**, *5* (8), 861−77.
(24) Cazalbou, S.; Bertrand, G.; Drouet, C. Tetracycline-Loaded Biomimetic Apatite: An Adsorption Study. *J. Phys. Chem. B* **2015**, *119*, 3014.
(25) Liu, W. C.; Wong, C. T.; Fong, M. K.; Cheung, W. S.; Kao, R. Y. T.; Luk, K. D. K.; Lu, W. W. Gentamicin-loaded strontium-containing hydroxyapatite bioactive bone cement-An efficient bioactive antibiotic drug delivery system. *J. Biomed. Mater. Res., Part B* **2010**, *95B* (2), 397−406.
(26) Kim, H. W.; Knowles, J. C.; Kim, H. E. Porous scaffolds of gelatin-hydroxyapatite nanocomposites obtained by biomimetic approach: characterization and antibiotic drug release. *J. Biomed. Mater. Res., Part B* **2005**, *74* (2), 686−98.

(27) Iafisco, M.; Delgado-Lopez, J. M.; Varoni, E. M.; Tampieri, A.; Rimondini, L.; Gomez-Morales, J.; Prat, M. Cell Surface Receptor Targeted Biomimetic Apatite Nanocrystals for Cancer Therapy. *Small* **2013**, *9* (22), 3834−3844.
(28) Pascaud, P.; Errassifi, F.; Brouillet, F.; Sarda, S.; Barroug, A.; Legrouri, A.; Rey, C. Adsorption on apatitic calcium phosphates for drug delivery: interaction with bisphosphonate molecules. *J. Mater. Sci.: Mater. Med.* **2014**, *25* (10), 2373−2381.
(29) Palazzo, B.; Iafisco, M.; Laforgia, M.; Margiotta, N.; Natile, G.; Bianchi, C. L.; Walsh, D.; Mann, S.; Roveri, N. Biomimetic hydroxyapatite-drug nanocrystals as potential bone substitutes with antitumor drug delivery properties. *Adv. Funct. Mater.* **2007**, *17* (13), 2180−2188.
(30) Iafisco, M.; Drouet, C.; Adamiano, A.; Pascaud, P.; Montesi, M.; Panseri, S.; Sarda, S.; Tampieri, A. Superparamagnetic iron-doped nanocrystalline apatite as a delivery system for doxorubicin. *J. Mater. Chem. B* **2016**, *4* (1), 57−70.
(31) Rodriguez-Ruiz, I.; Delgado-Lopez, J. M.; Duran-Olivencia, M. A.; Iafisco, M.; Tampieri, A.; Colangelo, D.; Prat, M.; Gomez-Morales, J. pH-Responsive Delivery of Doxorubicin from Citrate-Apatite Nanocrystals with Tailored Carbonate Content. *Langmuir* **2013**, *29* (26), 8213−8221.
(32) Iafisco, M.; Margiotta, N. Silica xerogels and hydroxyapatite nanocrystals for the local delivery of platinum-bisphosphonate complexes in the treatment of bone tumors: A mini-review. *J. Inorg. Biochem.* **2012**, *117*, 237−247.
(33) Hossain, S.; Yamamoto, H.; Chowdhury, E. H.; Wu, X.; Hirose, H.; Haque, A.; Doki, Y.; Mori, M.; Akaike, T. Fabrication and Intracellular Delivery of Doxorubicin/Carbonate Apatite Nanocomposites: Effect on Growth Retardation of Established Colon Tumor. *PLoS One* **2013**, *8* (4), e60428.
(34) Sarda, S.; Errassifi, F.; Marsan, O.; Geffre, A.; Trumel, C.; Drouet, C. Adsorption of tranexamic acid on hydroxyapatite: Toward the development of biomaterials with local hemostatic activity. *Mater. Sci. Eng., C* **2016**, *66*, 1−7.
(35) Weber, C. G.; Mueller, M.; Vandecandelaere, N.; Trick, I.; Burger-Kentischer, A.; Maucher, T.; Drouet, C. Enzyme-functionalized biomimetic apatites: concept and perspectives in view of innovative medical approaches. *J. Mater. Sci.: Mater. Med.* **2014**, *25* (3), 595−606.
(36) Grunenwald, A.; Keyser, C.; Sautereau, A. M.; Crubezy, E.; Ludes, B.; Drouet, C. Adsorption of DNA on biomimetic apatites: Toward the understanding of the role of bone and tooth mineral on the preservation of ancient DNA. *Appl. Surf. Sci.* **2014**, *292*, 867−875.
(37) Mondejar, S. P.; Kovtun, A.; Epple, M. Lanthanide-doped calcium phosphate nanoparticles with high internal crystallinity and with a shell of DNA as fluorescent probes in cell experiments. *J. Mater. Chem.* **2007**, *17* (39), 4153−4159.
(38) Chowdhury, E. H.; Akaike, T. Advances in fabrication of calcium phosphate nano-composites for smart delivery of DNA and RNA to mammalian cells. *Curr. Anal. Chem.* **2005**, *1* (2), 187−192.
(39) Hammami, K.; El-Feki, H.; Marsan, O.; Drouet, C. Adsorption of nucleotides on biomimetic apatite: The case of adenosine 5 ' triphosphate (ATP). *Appl. Surf. Sci.* **2016**, *360*, 979−988.
(40) Hammami, K.; El Feki, H.; Marsan, O.; Drouet, C. Adsorption of nucleotides on biomimetic apatite: The case of adenosine 5 ' monophosphate (AMP). *Appl. Surf. Sci.* **2015**, *353*, 165−172.
(41) Choimet, M.; Tourrette, A.; Drouet, C. Adsorption of nucleotides on biomimetic apatite: The case of cytidine 5 ' monophosphate (CMP). *J. Colloid Interface Sci.* **2015**, *456*, 132−137.
(42) Stefanic, M.; Ward, K.; Tawfik, H.; Seemann, R.; Baulin, V.; Guo, Y.; Fleury, J.-B.; Drouet, C. Apatite nanoparticles strongly improve red blood cell cryopreservation by mediating trehalose delivery via enhanced membrane permeation. *Biomaterials* **2017**, *140*, 138−149.
(43) Tampieri, A.; D'Alessandro, T.; Sandri, M.; Sprio, S.; Landi, E.; Bertinetti, L.; Panseri, S.; Pepponi, G.; Goettlicher, J.; Banobre-Lopez, M.; Rivas, J. Intrinsic magnetism and hyperthermia in bioactive Fe-doped hydroxyapatite. *Acta Biomater.* **2012**, *8* (2), 843−851.
(44) Iannotti, V.; Adamiano, A.; Ausanio, G.; Lanotte, L.; Aquilanti, G.; Coey, J. M. D.; Lantieri, M.; Spina, G.; Fittipaldi, M.; Margaris, G.; Trohidou, K.; Sprio, S.; Montesi, M.; Panseri, S.; Sandri, M.; Iafisco, M.; Tampieri, A. Fe-Doping-Induced Magnetism in Nano-Hydroxyapatites. *Inorg. Chem.* **2017**, *56* (8), 4446−4458.
(45) Adamiano, A.; Iafisco, M.; Sandri, M.; Basini, M.; Arosio, P.; Canu, T.; Sitia, G.; Esposito, A.; Iannotti, V.; Ausanio, G.; Fragogeorgi, E.; Rouchota, M.; Loudos, G.; Lascialfari, A.; Tampieri, A. On the use of superparamagnetic hydroxyapatite nanoparticles as an agent for magnetic and nuclear in vivo imaging. *Acta Biomater.* **2018**, *73*, 458.
(46) Toffoli, G.; Cernigoi, C.; Russo, A.; Gallo, A.; Bagnoli, M.; Boiocchi, M. Overexpression of folate binding protein in ovarian cancers. *Int. J. Cancer* **1997**, *74* (2), 193−198.
(47) Santos, C.; Gomes, P.; Duarte, J. A.; Almeida, M. M.; Costa, M. E. V.; Fernandes, M. H. Development of hydroxyapatite nanoparticles loaded with folic acid to induce osteoblastic differentiation. *Int. J. Pharm.* **2017**, *516* (1), 185−195.
(48) Sun, C.; Sze, R.; Zhang, M. Folic acid-PEG conjugated superparamagnetic nanoparticles for targeted cellular uptake and detection by MRI. *J. Biomed. Mater. Res., Part A* **2006**, *78* (3), 550−7.
(49) Drouet, C.; Al-Kattan, A.; Choimet, M.; Tourrette, A.; Santran, V.; Dexpert-Ghys, J.; Pipy, B.; Brouillet, F.; Tourbin, M. Biomimetic Apatite-Based Functional Nanoparticles as Promising Newcomers in Nanomedicine: Overview of 10 Years of Initiatory Research. *IMPH* **2015**, *1* (1), 1−9.
(50) Cipreste, M. F.; Gonzalez, I.; Maria da Mata Martins, T.; Goes, A. M.; Augusto de Almeida Macedo, W.; Barros de Sousa, E. M. Attaching folic acid on hydroxyapatite nanorod surfaces: an investigation of the HA-FA interaction. *RSC Adv.* **2016**, *6* (80), 76390−76400.
(51) Kohler, N.; Sun, C.; Wang, J.; Zhang, M. Methotrexate-modified superparamagnetic nanoparticles and their intracellular uptake into human cancer cells. *Langmuir* **2005**, *21* (19), 8858−64.
(52) Tampieri, A.; D'Alessandro, T.; Sandri, M.; Sprio, S.; Landi, E.; Bertinetti, L.; Panseri, S.; Pepponi, G.; Goettlicher, J.; Bañobre-López, M.; Rivas, J. Intrinsic magnetism and hyperthermia in bioactive Fe-doped hydroxyapatite. *Acta Biomater.* **2012**, *8* (2), 843−851.
(53) Patterson, A. L. The scherrer formula for X-ray particle size determination. *Phys. Rev.* **1939**, *56* (10), 978−982.
(54) Fassina, L.; Visai, L.; Benazzo, F.; Benedetti, L.; Calligaro, A.; Cusella De Angelis, M. G.; Farina, A.; Maliardi, V.; Magenes, G. Effects of electromagnetic stimulation on calcified matrix production by SAOS-2 cells over a polyurethane porous scaffold. *Tissue Eng.* **2006**, *12* (7), 1985−1999.
(55) Castillo, J. J.; Rindzevicius, T.; Rozo, C. E.; Boisen, A. Adsorption and Vibrational Study of Folic Acid on Gold Nanopillar Structures Using Surface-Enhanced Raman Scattering Spectroscopy. *Nanomater. Nanotechnol.* **2015**, *5*, 29.
(56) Kokaislová, A.; Helešicová, T.; Ončák, M.; Matějka, P. Spectroscopic studies of folic acid adsorbed on various metal substrates: does the type of substrate play an essential role in temperature dependence of spectral features? *J. Raman Spectrosc.* **2014**, *45* (9), 750−757.
(57) Penel, G.; Leroy, G.; Rey, C.; Bres, E. MicroRaman spectral study of the PO4 and CO3 vibrational modes in synthetic and biological apatites. *Calcif. Tissue Int.* **1998**, *63* (6), 475−481.
(58) Rey, C.; Marsan, O.; Combes, C.; Drouet, C.; Grossin, D.; Sarda, S. Characterization of Calcium Phosphates Using Vibrational Spectroscopies. In *Advances in Calcium Phosphate Biomaterials*, Ben-Nissan, B., Ed.; Springer: Berlin, Heidelberg, 2014; Vol. 2, pp 229−266.
(59) Rollin-Martinet, S.; Navrotsky, A.; Champion, E.; Grossin, D.; Drouet, C. Thermodynamic basis for evolution of apatite in calcified tissues. *Am. Mineral.* **2013**, *98*, 2037−2045.
(60) Choy, J. H.; Jung, J. S.; Oh, J. M.; Park, M.; Jeong, J.; Kang, Y. K.; Han, O. J. Layered double hydroxide as an efficient drug reservoir for folate derivatives. *Biomaterials* **2004**, *25* (15), 3059−64.

(61) Oh, J.-M.; Park, M.; Kim, S.-T.; Jung, J.-Y.; Kang, Y.-G.; Choy, J.-H. Efficient delivery of anticancer drug MTX through MTX-LDH nanohybrid system. *J. Phys. Chem. Solids* **2006**, *67* (5), 1024−1027.
(62) Meshkini, A.; Oveisi, H. Methotrexate-F127 conjugated mesoporous zinc hydroxyapatite as an efficient drug delivery system for overcoming chemotherapy resistance in osteosarcoma cells. *Colloids Surf., B* **2017**, *158*, 319−330.

Supporting Information:

Interaction of folic acid with nanocrystalline apatites and extension to methotrexate (antifolate) in view of anticancer applications

Stephanie Sarda‡, Michele Iafisco†*, Patricia Pascaud‡§, Alessio Adamiano†, Monica Montesi†, Silvia Panseri†, Olivier Marsan‡, Carole Thouron‡, Agnès Dupret-Bories‡♯, Anna Tampieri† and Christophe Drouet‡†**

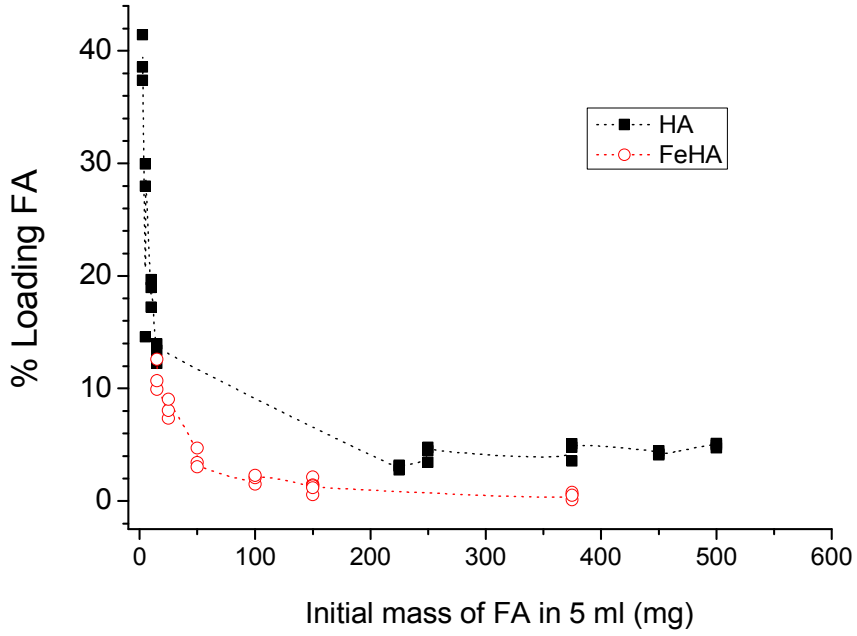

Figure SI1. Evolution of FA loading percentage versus initial contacted amount in solution

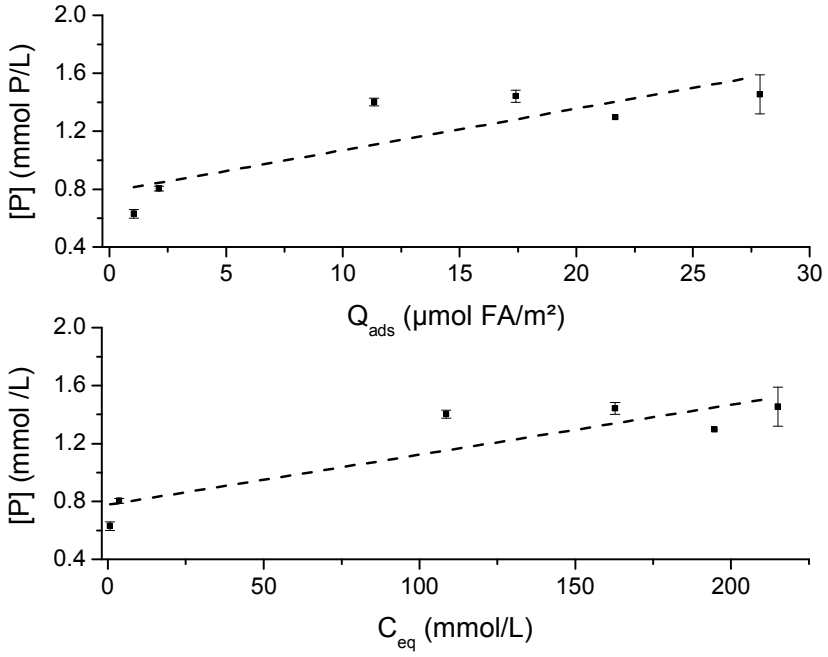

Figure SI2. Evolution of phosphate concentration in the supernatant after FA adsorption on nanocrystalline apatite HA

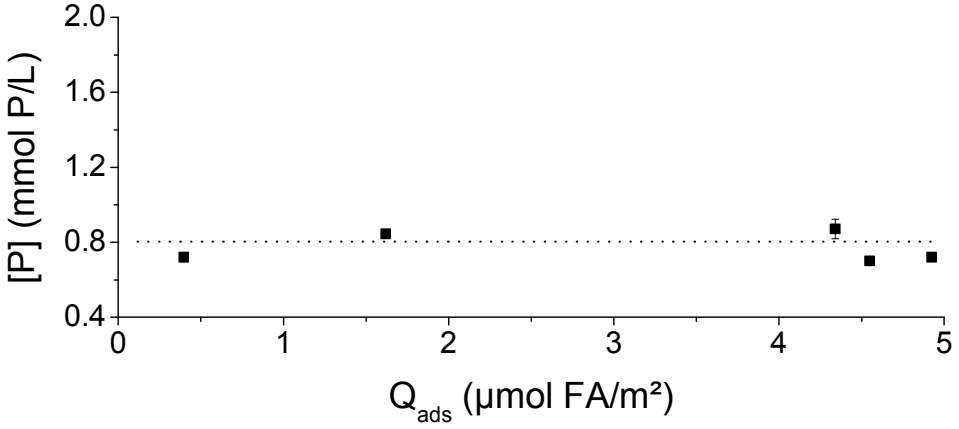

Figure SI3. Evolution of phosphate concentration in the supernatant after FA adsorption on iron-containing nanocrystalline apatite FeHA

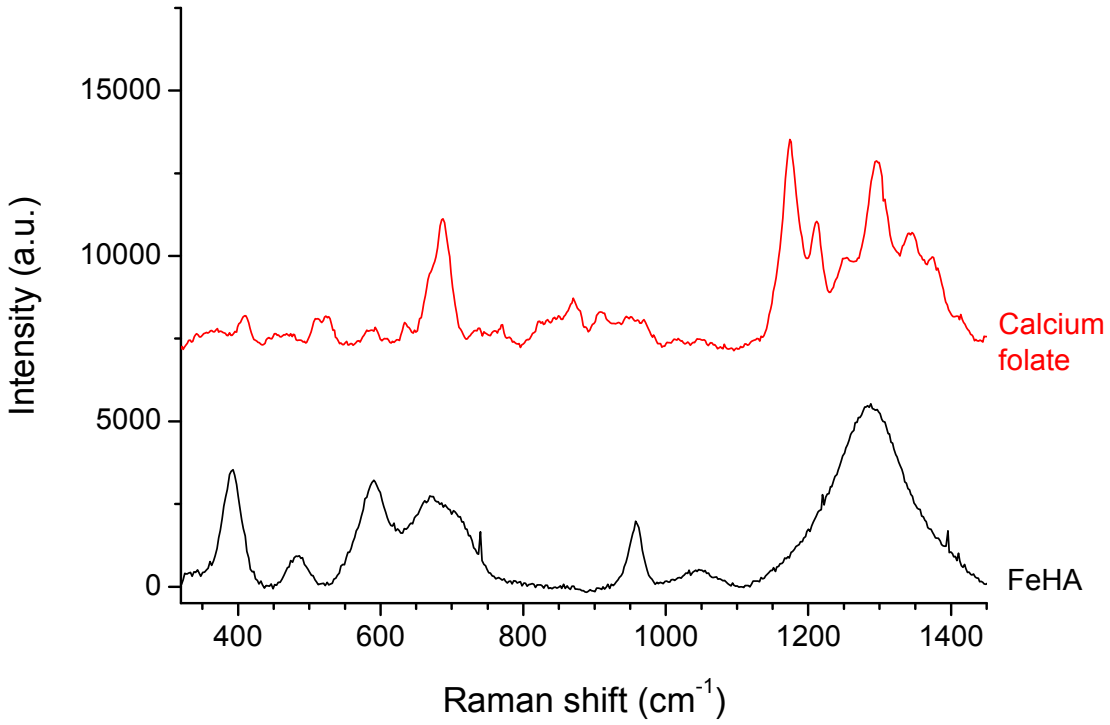

Figure SI4. Raman spectra of FeHA (part rich in iron oxide) and calcium folate

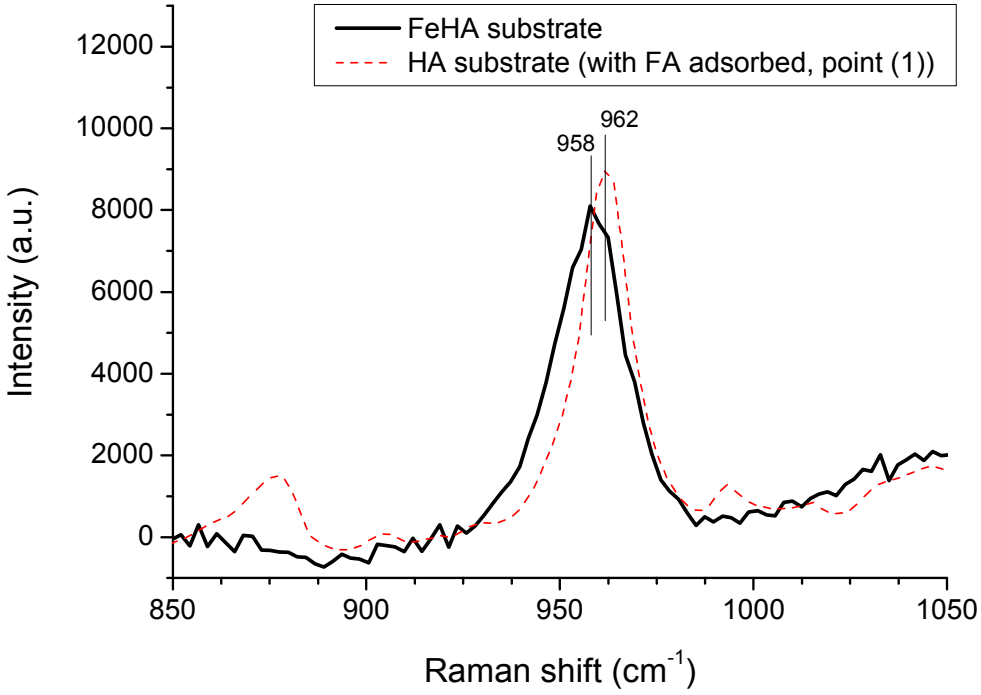

Figure SI5. Raman spectral detail around the $\nu_1(PO_4)$ mode of the apatite phase in FeHA as compared to HA

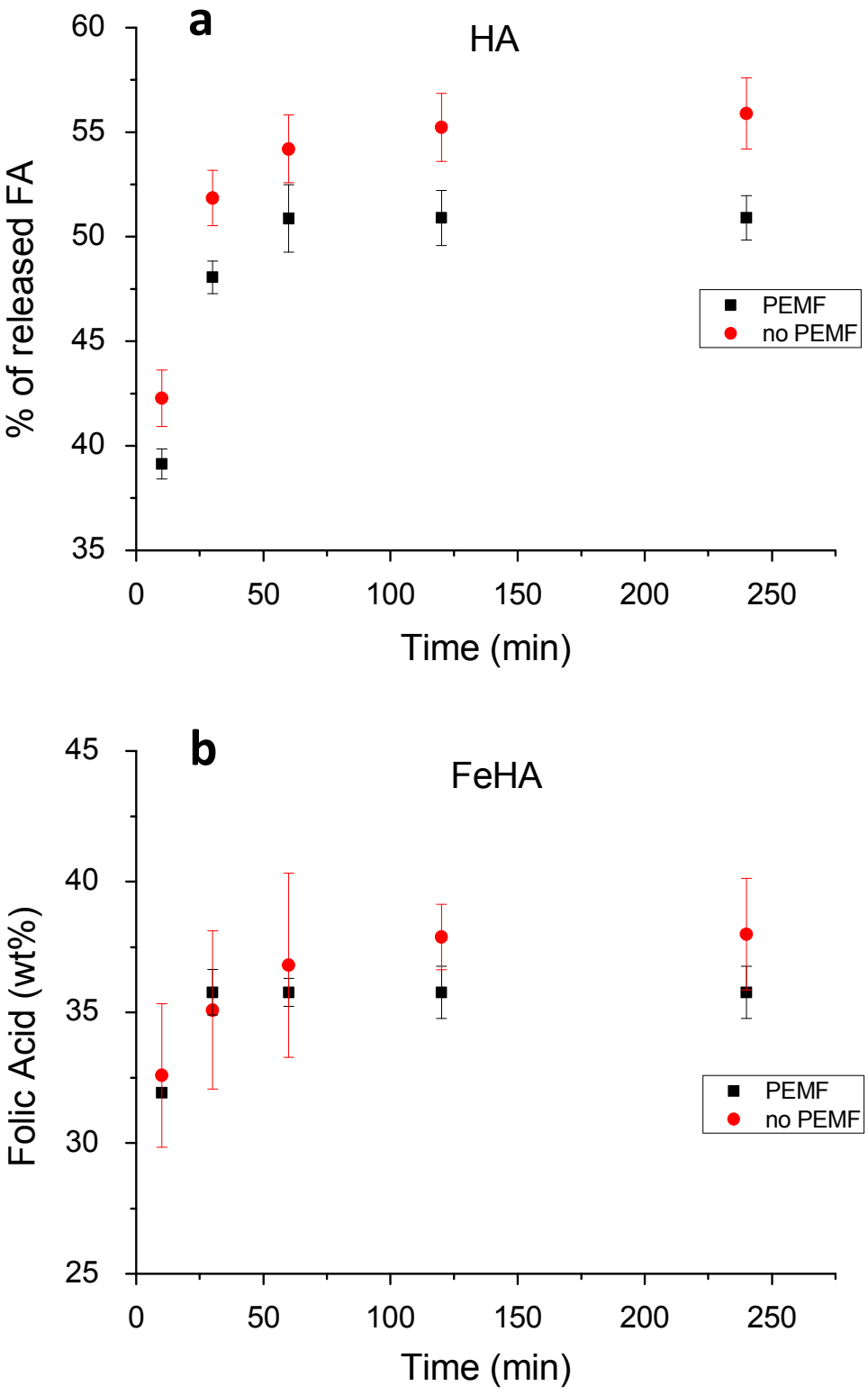

Figure SI6. FA desorption kinetics at early time points on HA (a) and FeHA (b), in the presence or absence of external magnetic field (PEMF)

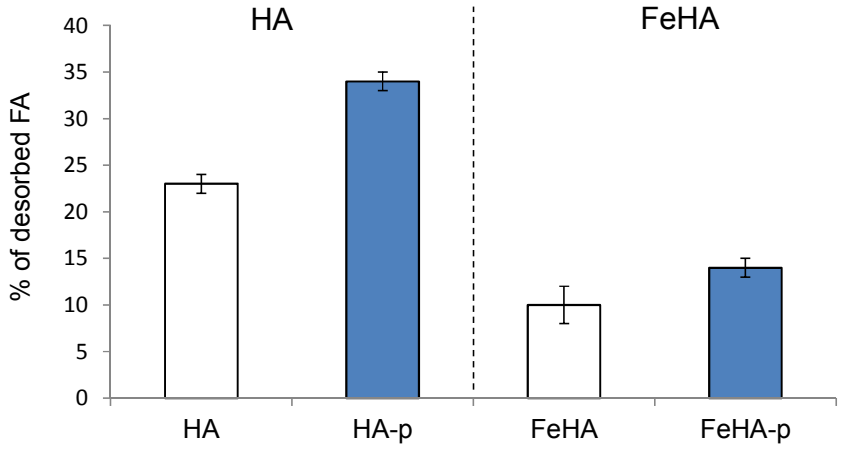

Figure SI7. Desorption tests at 37°C, at t = 1.5 h, in NaCl 0.9 wt.%, in the absence or presence (denoted "p") of KH_2PO_4 0.02 M

Figure SI8. Histology data after implantation of HA and FeHA in mice (3 weeks). Both Hematoxyline-Eosine (HA) and Masson trichrome stainings are shown with small (x5) and larger (x10) views

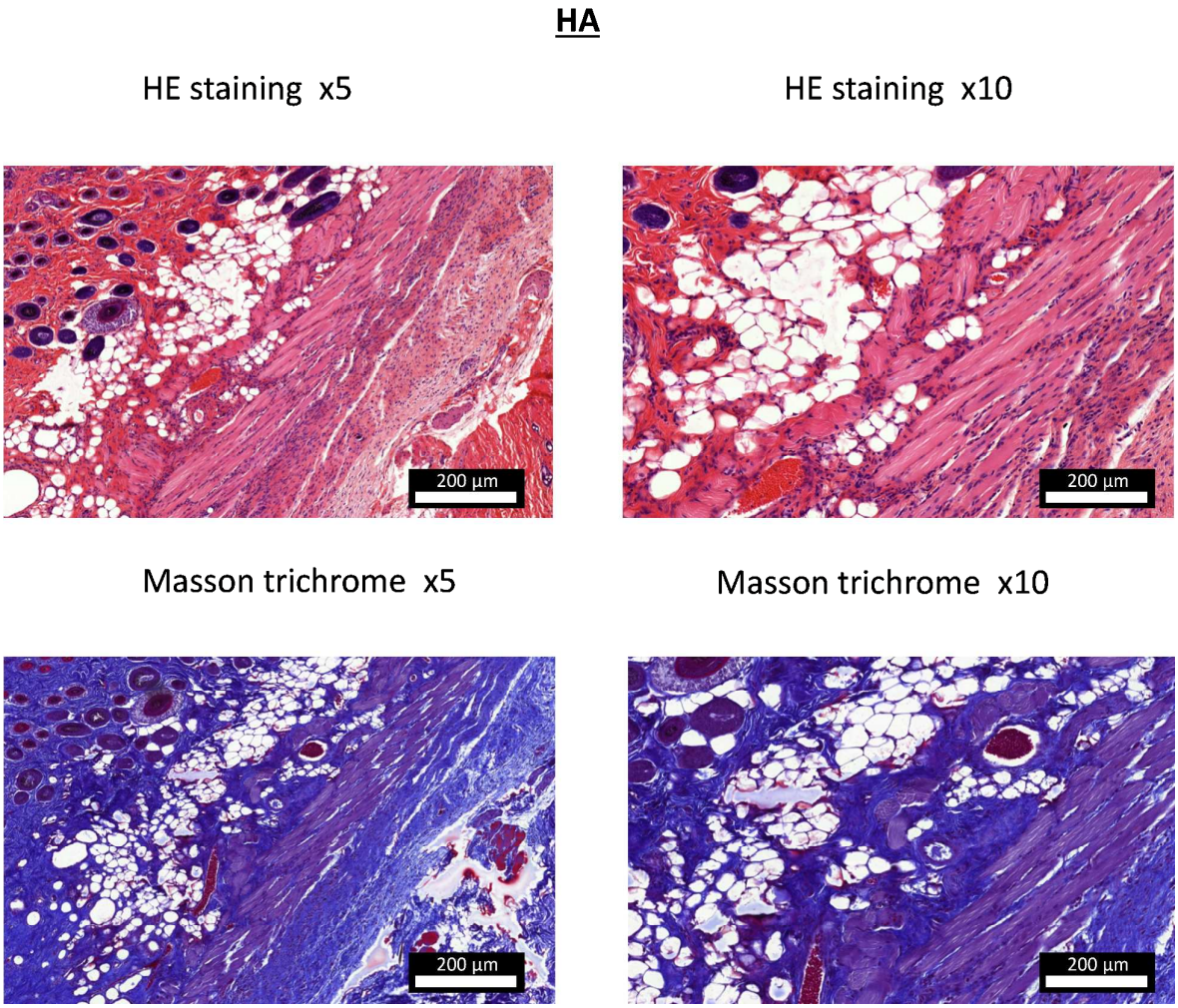

FeHA

HE staining x5

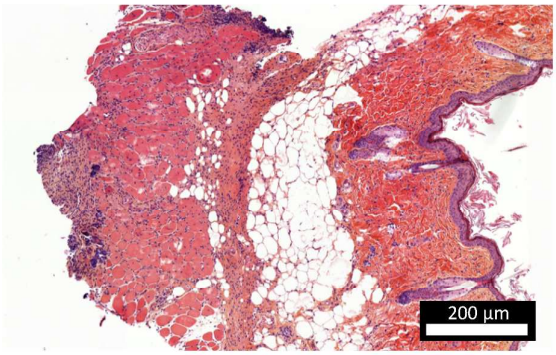

HE staining x10

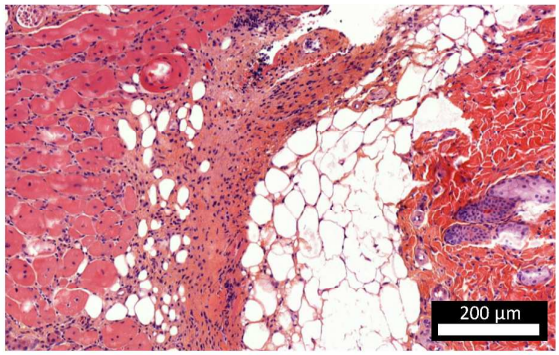

Masson trichrome x5

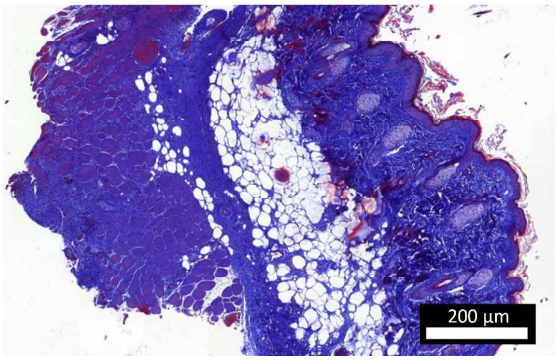

Masson trichrome x10

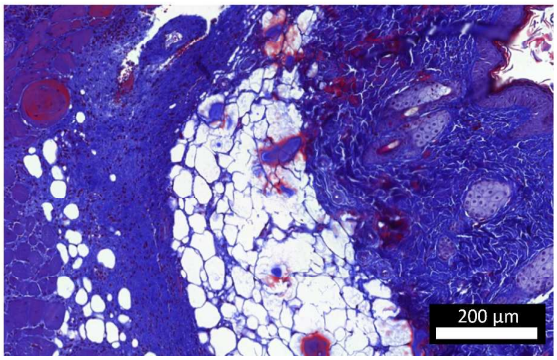

Table SI1. Experimental conditions for *in vitro* tests using MTX

Samples	MTX loaded on HA or FeHA (µg/mg)	MTX µg/ml tested	HA or FeHA µg/ml
HA-MTX 50µM	101.8	22,7	228
HA Ct_1	-	-	228
HA-MTX 5µM	101.8	2,27	22,8
HA Ct_2	-	-	22,8
FeHA-MTX 50µM	99.6	22,7	223
FeHA Ct_1	-	-	223
FeHA-MTX 5µM	99.6	2,27	22,3
FeHA Ct_2	-	-	22,3
MTX 50µM	-	22,7	-
MTX 5µM	-	2,27	-